A study of the non-linear properties and wave generation of the multi-layer non-hydrostatic wave model SWASH

Vasarmidis, Panagiotis; Klonaris, Georgios; Zijlema, Marcel; Stratigaki, Vasiliki; Troch, Peter

DOI
10.1016/j.oceaneng.2024.117633

Publication date
2024

Document Version
Final published version

Published in
Ocean Engineering

Citation (APA)
Vasarmidis, P., Klonaris, G., Zijlema, M., Stratigaki, V., & Troch, P. (2024). A study of the non-linear properties and wave generation of the multi-layer non-hydrostatic wave model SWASH. *Ocean Engineering*, *302*, Article 117633. https://doi.org/10.1016/j.oceaneng.2024.117633

Ocean Engineering 302 (2024) 117633

Contents lists available at ScienceDirect

Ocean Engineering

journal homepage: www.elsevier.com/locate/oceaneng

A study of the non-linear properties and wave generation of the multi-layer non-hydrostatic wave model SWASH

Panagiotis Vasarmidis [a,*], Georgios Klonaris [a], Marcel Zijlema [b], Vasiliki Stratigaki [a], Peter Troch [a]

[a] Department of Civil Engineering, Ghent University, Technologiepark 60, 9052, Zwijnaarde, Belgium
[b] Department of Hydraulic Engineering, Delft University of Technology, Stevinweg 1, 2628 CN, Delft, The Netherlands

ARTICLE INFO

Keywords:
Non-hydrostatic model
SWASH
Linear and non-linear properties
Sub- and super-harmonics
Improved wave generation

ABSTRACT

Despite the increasing use of non-hydrostatic models in the study of wave processes in coastal regions, there is still limited understanding of the non-linear properties of the governing equations and how they improve with increased vertical resolution. In this study, the governing equations of the non-hydrostatic wave model SWASH are analysed and the linear and non-linear solutions up to third-order of all dependent variables are derived, considering one to four vertical layers. The analysis concludes that the model can achieve excellent non-linear properties with respect to the Stokes theory over a large range of water depths using only a few vertical layers. Furthermore, deriving solutions for all variables enables the formulation of improved wave generation and absorption boundary conditions for non-hydrostatic models. A well-known issue of non-linear wave models is related to the generation and propagation of spurious free waves, resulting to non-homogeneous wave fields. In this study, it is proven that by imposing the derived exact mathematical solutions of the governing equations at the model's boundaries, the target first- and second-order wave profiles can be generated with high accuracy, while the spurious waves can be entirely eliminated.

1. Introduction

Phase-resolving numerical models have been already utilised for more than three decades to predict the wave transformation in coastal environments. Nowadays that the vulnerability of these environments is increased due to climate change and the resulting intensity of storms, the importance of the accuracy of the models' predictions is significant. Research efforts are focused on extending the capabilities of the numerical models by limiting the assumptions in the derivation of the governing equations but maintaining the computational cost as low as possible.

Some of the earliest phase-resolving models were based on the non-linear shallow water equations (NLSWE). These models assume that the non-linear effects dominate over the dispersive effects and their applicability is focused on the inner region of the surf zone and particularly on wave run-up (Hibberd and Peregrine, 1979; Kobayashi et al., 1987; Kobayashi and Wurjanto, 1992; Brocchini and Peregrine, 1996; Hu et al., 2000). However, outside the surf zone in the pre-breaking region NLSWE models are not valid since a hydrostatic pressure distribution is assumed (Svendsen, 2005). The front face of propagating waves, even over a flat bottom, is continuously steepening until a vertical front shape is reached (Peregrine, 1972). To stabilise the continuous steepening of the free surface, a non-hydrostatic pressure component needs to be included in the governing equations (Svendsen and Madsen, 1984).

In Boussinesq equations (BE) models, the effect of the non-hydrostatic component is incorporated by adding higher-order derivative terms in the NLSWE. The classical form of Boussinesq equations was derived by Peregrine (1967), who assumed that dispersive and non-linear effects are of equal importance, and was able to describe long waves with small amplitude propagating over uneven bottoms. Thus, these equations were characterised as weakly non-linear and weakly dispersive and were applicable up to dimensionless depths, kd, of 0.75, where k and d are the wave number and still water depth, respectively. Since their inception, research efforts have been dedicated to deriving and extending Boussinesq-type equations with enhanced linear and non-linear properties. Madsen et al. (1991) and Madsen and Sørensen (1992) extended the applicability of the Peregrine (1967) equations to deeper water by using a Padé approximation and introducing additional third-order terms in the governing equations. Following a different approach, Nwogu (1993) achieved similar dispersive properties by defining the horizontal velocity component at an arbitrary level with respect to the vertical axis. Later, Wei et al. (1995) derived a fully non-linear Boussinesq-type wave model based on the Nwogu (1993) formulation. Since then, high-order Boussinesq-type models have been developed to further improve the linear and

* Corresponding author.
E-mail address: panagiotis.vasarmidis@ugent.be (P. Vasarmidis).

https://doi.org/10.1016/j.oceaneng.2024.117633
Received 6 January 2024; Received in revised form 22 March 2024; Accepted 22 March 2024
Available online 27 March 2024

non-linear effects (Klonaris et al., 2016), either through the use of higher-order polynomial approximations for the vertical distribution of the flow field (Gobbi et al., 2000; Castro-Orgaz et al., 2022b) or in terms of a multi-layer concept (Lynett and Liu, 2004a; Liu et al., 2018). However, the use of high-order cross derivatives in time and space adds to the mathematical complexity of Boussinesq-type models and leads to an increased computational cost and potential numerical instabilities.

In order to overcome these demanding numerical treatments, several alternatives for the solution of the equivalent non-hydrostatic pressure system have been proposed. Many of them rely on the mathematical background of the Serre-Green–Naghdi (SGN) equations (Green and Naghdi, 1976), which typically employ expansions of the velocity vector in terms of some basis functions. Since the 3D flow equations cannot satisfy these expansions, integral expressions are adopted, resulting in variational methods. This approach is equivalent to the method of weighted residuals, which, in combination with high-level versions of SGN theory, results in increased accuracy (Zhao et al., 2014; Yang and Liu, 2020). Castro-Orgaz et al. (2022a) presented a method to derive higher-order non-hydrostatic equations combining the usual dispersive corrections of SGN equations with higher-order velocity profile corrections. The solution of the proposed set of equations was accomplished through a numerical scheme of increased stability, resulting to a model of pronounced efficiency for wave propagation over abrupt obstacles.

Over the past two decades, a different route has been taken with the development of the non-hydrostatic wave models. This approach has been pursued with the purpose of preventing the introduction of unwanted high-order derivative terms. It constitutes a numerical implementation of the Navier–Stokes equations for an incompressible fluid with a free surface and a constant density. Casulli and Stelling (1998) proposed a time-splitting integration method to solve the 3D Reynolds-Averaged Navier–Stokes (RANS) equations, according to which the velocity field is at first predicted assuming the hydrostatic problem, and subsequently the wave field is corrected in response to the non-hydrostatic pressure correction obtained by solving a Poisson-type equation. Although the first non-hydrostatic models required a similar to BE models horizontal grid resolution, a very fine resolution over the vertical direction (typically ranging from 10 to 20 layers) was needed to achieve a satisfactory level of accuracy in resolving frequency dispersion. As a result, the computational cost of non-hydrostatic models was much higher compared to BE models. Stelling and Zijlema (2003) and Zijlema and Stelling (2005) introduced a Keller Box scheme for the discretisation of the pressure over the vertical direction, while Zijlema and Stelling (2008) proved that this Keller Box scheme leads to better dispersive properties than the central differences scheme when a coarse vertical resolution is applied. More precisely, by utilising a layout of two layers the model was able to resolve linear dispersive waves up to kd values of 7.7 with a maximum relative error of only 1%. After these recent developments, several non-hydrostatic wave models have been developed (Zijlema et al., 2011; Yamazaki et al., 2011; Ai et al., 2011; Ma et al., 2012). By retaining the 3D momentum equations non-hydrostatic models can directly compute the vertical and horizontal flow structure, while the computational effort is similar to the BE models. Additionally, they are prone to less numerical instabilities compared to the BE models due to the absence of higher-order cross derivatives of the dependent variables in the governing equations.

The multi-layer non-hydrostatic model SWASH has undoubtedly attained an advanced stage in the field of wave transformation in coastal environments. This is due to its ability to incorporate various non-linear shallow-water effects, including bound sub-harmonics, super-harmonics, and near-resonant triad interactions (Rijnsdorp et al., 2014, 2015; Smit et al., 2014). The model has been recently employed in various applications, such as the study of wave overtopping (Suzuki et al., 2017), wave penetration (Dobrochinski et al., 2023), wave-induced currents (Rijnsdorp et al., 2017), and the examination of wave interactions with vegetation (Suzuki et al., 2019) and floating bodies (Rijnsdorp et al., 2018, 2022). However, despite the existence of numerous applications for non-hydrostatic wave models, there is still limited insight into the nonlinear solutions of the governing equations and how these solutions can be utilised to improve and extend the wave generation capabilities of these models.

A well-known issue in non-linear wave models is related to the generation and propagation of spurious free waves, resulting in non-homogeneous wave fields. The main objective of the present study focuses on improving the wave generation boundary conditions of non-hydrostatic wave models, aiming to enhance the capabilities of these models and, consequently, improve the accuracy of the aforementioned applications. To achieve this objective, the governing equations of the non-hydrostatic wave model SWASH are analysed, both for examining their linear and non-linear properties and for defining improved wave generation boundary conditions. A Stokes-type Fourier analysis is performed over a flat bottom to derive higher-order solutions based on the model equations. This kind of analysis has served as a standard tool for defining and comparing the linear and non-linear properties of different Boussinesq and non-hydrostatic wave models (Madsen and Sørensen, 1993; Madsen and Schäffer, 1998; Memos et al., 2016; Lynett and Liu, 2004b; Gobbi et al., 2000; Bai and Cheung, 2013; Wang et al., 2018, 2019; Escalante et al., 2023; Castro-Orgaz et al., 2023). In the present study, this analysis is performed for all the dependent variables up to third-order. The layer-integrated version of the governing equations is applied, considering one to four vertical layers, while the dimensionless water depth range over which the model achieves the target accuracy for each variable is defined. Deriving solutions for all variables enables the formulation of improved wave generation and absorption boundary conditions for non-hydrostatic models. It is demonstrated in this study that by imposing the derived exact mathematical solutions of the governing equations at the model's boundaries, the target wave profiles can be generated with high accuracy, while the spurious waves can be entirely eliminated. To the best of the authors' knowledge, the proposed approach has not been employed in the past for non-hydrostatic models and, therefore, highlights the novelty of the present work.

The paper is structured as follows. Section 2 provides a description of the layer-integrated governing equations of the multi-layer non-hydrostatic model SWASH. In Section 3.1, the linearised equations and first-order solutions are derived. Subsequent sections focus on providing a detailed presentation of the non-linear properties of the SWASH model. More precisely, the second- and third-order equations are defined and the corresponding solutions are derived in Sections 3.2 and 3.3, respectively. Additionally, Section 3.4 presents the derivation of second-order transfer functions for sub-harmonic and super-harmonic interactions. In Section 4, the derived expressions are used to formulate improved wave generation boundary conditions, and the results are compared with analytical solutions. Finally, the conclusions of this study are included in the last section.

2. Theory

2.1. Governing equations

The SWASH (https://swash.sourceforge.io/) model (Zijlema et al., 2011) is an open-source multi-layer non-hydrostatic model based on the Euler equations describing an incompressible fluid with a free surface η and a constant density ρ_0. The Euler equations for a 2D-vertical domain where the water column is defined from the free-surface, $z = \eta$, to the bottom, $z = -d$, are given by:

$$\frac{\partial u}{\partial x} + \frac{\partial w}{\partial z} = 0 \tag{1}$$

$$\frac{\partial u}{\partial t} + \frac{\partial uu}{\partial x} + \frac{\partial uw}{\partial z} + \frac{\partial P}{\partial x} = 0 \tag{2}$$

$$\frac{\partial w}{\partial t} + \frac{\partial uw}{\partial x} + \frac{\partial ww}{\partial z} + \frac{\partial P}{\partial z} = -g \tag{3}$$

where u and w are, respectively, the horizontal and vertical velocities, g is the gravitational acceleration and P is the total pressure normalised with the reference density ρ_0. The total pressure is defined as:

$$P = p - gz = q + g(\eta - z) \tag{4}$$

where p and q are the dynamic and non-hydrostatic pressures, respectively. The two kinematic boundary conditions, one at the free surface and one at the impermeable bottom, are expressed as:

$$w_s = \frac{\partial \eta}{\partial t} + u\frac{\partial \eta}{\partial x} \qquad z = \eta \tag{5}$$

$$w_b = -u\frac{\partial d}{\partial x} \qquad z = -d \tag{6}$$

Integrating the continuity equation (Eq. (1)) over the entire water column, $h = d + \eta$, and applying the kinematic boundary conditions, the free surface equation can be obtained:

$$\frac{\partial \eta}{\partial t} + \frac{\partial}{\partial x}\int_{-d}^{\eta} u dz = 0 \tag{7}$$

In SWASH, a structured (rectilinear or orthogonal curvilinear) or an unstructured (Zijlema, 2020) grid can be applied in the horizontal direction, while in the vertical direction the water column is split into a fixed number of layers. The unknowns are arranged in a staggered grid, where the horizontal u and the vertical w velocity components are defined at the vertical and horizontal cell faces, respectively. Regarding the non-hydrostatic pressure two arrangements are possible: (a) the Keller Box scheme, where the pressure is defined at the cell face (same location as w) or (b) the central difference scheme, where the pressure is defined at the centre of the cell. As demonstrated by Zijlema and Stelling (2008), the Keller Box scheme leads to better linear dispersive properties than the central difference scheme when coarse vertical resolution is applied. Note that for a sufficiently fine vertical resolution, both the Keller Box scheme and the central difference scheme have similar dispersion properties, while the latter is more robust and, thus, preferable to apply (for details, see, e.g. Zijlema and Stelling, 2008; Smit et al., 2014). Since the objective of this paper is to study the transformation of dispersive waves, we therefore restrict our proposed analysis up to four layers with the use of the Keller Box scheme. However, we emphasise that SWASH can be employed for an arbitrary number of layers (see, e.g. Rijnsdorp et al., 2017) when the central difference scheme is applied.

In order to derive the governing equations for a system of any number of vertical layers, the layer-integrated Euler equations should be defined. By depth-integrating over each layer the governing non-hydrostatic Euler equations and applying the Leibniz integral rule, the layer-integrated continuity equation and momentum equations for layer k ($z_{k^-} \le z \le z_{k^+}$) can be obtained:

$$\frac{\partial h_k u_k}{\partial x} - u_{k^{(+)}}\frac{\partial z_{k^{(+)}}}{\partial x} + u_{k^{(-)}}\frac{\partial z_{k^{(-)}}}{\partial x} + w_{k^{(+)}} - w_{k^{(-)}} = 0 \tag{8}$$

$$\frac{\partial h_k u_k}{\partial t} + \frac{\partial h_k u_k u_k}{\partial x} + u_{k^{(+)}} w_{r,k^{(+)}} - u_{k^{(-)}} w_{r,k^{(-)}} + h_k g\frac{\partial \eta}{\partial x} + \frac{\partial h_k q_k}{\partial x} - q_{k^{(+)}}\frac{\partial z_{k^{(+)}}}{\partial x} + q_{k^{(-)}}\frac{\partial z_{k^{(-)}}}{\partial x} = 0 \tag{9}$$

$$\frac{\partial h_k w_k}{\partial t} + \frac{\partial h_k u_k w_k}{\partial x} + w_{k^{(+)}} w_{r,k^{(+)}} - w_{k^{(-)}} w_{r,k^{(-)}} + q_{k^{(+)}} - q_{k^{(-)}} = 0 \tag{10}$$

where w_r is the relative vertical velocity at the layer interface, defined as the difference between the vertical velocity along the streamline and the vertical velocity along the interface:

$$w_{r,k^{(+)}} = w_{k^{(+)}} - \frac{\partial z_{k^{(+)}}}{\partial t} - u_{k^{(+)}}\frac{\partial z_{k^{(+)}}}{\partial x} \tag{11}$$

A detailed step-by-step derivation of Eqs. (8)–(10) is given in Zijlema and Stelling (2005) and, thus, it is not included here.

2.2. System of equations for two vertical layers

The governing equations, the derivation procedure and the resulting expressions will be presented in detail for the case of two equidistant layers, while the extension to more layers is straightforward.

In Fig. 1, the definition sketch for the case of two equidistant vertical layers ($h_1 = h_2 = h/2$) and the location of the flow parameters with respect to z-axis are presented. As observed, a Keller Box scheme is considered for the pressures which are defined at the upper and lower boundaries of each layer (surface, interface and bottom). Additionally, the non-hydrostatic pressure at the free surface is $q_s = 0$ since the surface tension is neglected and the vertical velocity at the bottom is $w_b = 0$ since a flat bottom is considered ($\partial d/\partial x = 0$).

It has to be mentioned that another layer arrangement apart from the equidistant can be utilised to optimise the linear or non-linear properties of the model. However, optimising the layer arrangement to achieve a better representation of the linear wave dispersion will not necessarily result to a better representation of the non-linear properties as well and vice versa. Thus, the solutions for equidistant vertical layers are only presented here, since this is the most frequently used option in SWASH model applications.

Applying the layer-integrated equations (Eqs. (8)–(10)) for this two-layer system yields the following governing equations:

$$\frac{\partial \eta}{\partial t} + \frac{1}{2}\frac{\partial h(u_{k1} + u_{k2})}{\partial x} = 0 \tag{12}$$

$$\frac{1}{2}\frac{\partial h u_{k2}}{\partial x} - u_{k2}\frac{\partial \eta}{\partial x} + \frac{1}{4}(u_{k1} + u_{k2})\frac{\partial (h - 2d)}{\partial x} + w_s - w_{12} = 0 \tag{13}$$

$$\frac{1}{2}\frac{\partial h u_{k1}}{\partial x} - \frac{1}{4}(u_{k1} + u_{k2})\frac{\partial (h - 2d)}{\partial x} + w_{12} = 0 \tag{14}$$

$$\frac{1}{2}\frac{\partial h u_{k2}}{\partial t} + \frac{1}{2}\frac{\partial h u_{k2} u_{k2}}{\partial x} - \frac{1}{2}(u_{k1} + u_{k2}) w_{r,12} + \frac{1}{2} h g\frac{\partial \eta}{\partial x} + \frac{1}{4}\frac{\partial h q_{12}}{\partial x} + \frac{1}{2} q_{12}\frac{\partial (h - 2d)}{\partial x} = 0 \tag{15}$$

$$\frac{1}{2}\frac{\partial h u_{k1}}{\partial t} + \frac{1}{2}\frac{\partial h u_{k1} u_{k1}}{\partial x} + \frac{1}{2}(u_{k1} + u_{k2}) w_{r,12} + \frac{1}{2} h g\frac{\partial \eta}{\partial x} + \frac{1}{4}\frac{\partial h (q_{12} + q_b)}{\partial x} - \frac{1}{2} q_{12}\frac{\partial (h - 2d)}{\partial x} - q_b\frac{\partial d}{\partial x} = 0 \tag{16}$$

$$\frac{1}{4}\frac{\partial h(w_s + w_{12})}{\partial t} + \frac{1}{4}\frac{\partial h u_{k2}(w_s + w_{12})}{\partial x} - w_{r,12} w_{12} - q_{12} = 0 \tag{17}$$

$$\frac{1}{4}\frac{\partial h w_{12}}{\partial t} + \frac{1}{4}\frac{\partial h u_{k1} w_{12}}{\partial x} + w_{r,12} w_{12} + q_{12} - q_b = 0 \tag{18}$$

where u_{k2} and u_{k1} are the horizontal velocities of the top and the bottom layer, q_{12} and q_b are the non-hydrostatic pressures at the two layers' interface and the bottom, w_s and w_{12} are the vertical velocities at the free surface and the two layers' interface, and $w_{r,12}$ is the relative vertical velocity defined as:

$$w_{r,12} = w_{12} - \frac{1}{2}\frac{\partial (h - 2d)}{\partial t} - \frac{1}{4}(u_{k1} + u_{k2})\frac{\partial (h - 2d)}{\partial x} \tag{19}$$

For a system of two vertical layers ($K = 2$), there are seven equations ($3K + 1$) with seven unknowns: one free surface equation (Eq. (12)), two continuity equations (Eqs. (13) and (14)), two horizontal (Eqs. (15) and (16)) and two vertical (Eqs. (17) and (18)) momentum equations.

3. Linear and non-linear properties

In order to determine the linear and non-linear properties of the SWASH model, the first-, second- and third-order equations are derived

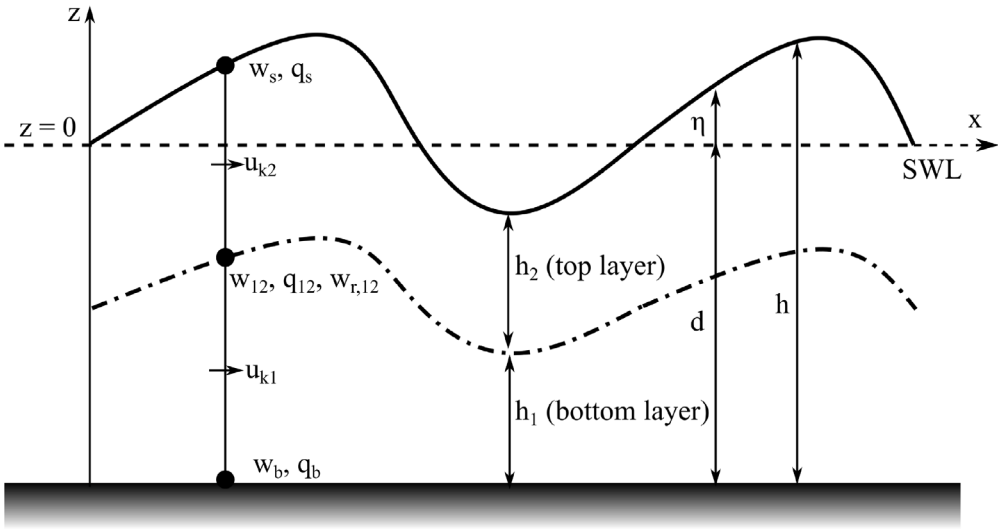

Fig. 1. Definition sketch for the case of two vertical layers and positioning of flow parameters with respect to z-axis.

through perturbation expansions, which in the case of two layers are given by:

$$\left.\begin{aligned} u_{k1} &= \epsilon u_{k1}^{(1)} + \epsilon^2 u_{k1}^{(2)} + \epsilon^3 u_{k1}^{(3)}, & u_{k2} &= \epsilon u_{k2}^{(1)} + \epsilon^2 u_{k2}^{(2)} + \epsilon^3 u_{k2}^{(3)}, \\ w_s &= \epsilon w_s^{(1)} + \epsilon^2 w_s^{(2)} + \epsilon^3 w_s^{(3)}, & w_{12} &= \epsilon w_{12}^{(1)} + \epsilon^2 w_{12}^{(2)} + \epsilon^3 w_{12}^{(3)}, \\ q_{12} &= \epsilon q_{12}^{(1)} + \epsilon^2 q_{12}^{(2)} + \epsilon^3 q_{12}^{(3)}, & q_b &= \epsilon q_b^{(1)} + \epsilon^2 q_b^{(2)} + \epsilon^3 q_b^{(3)}, \\ \eta &= \epsilon \eta^{(1)} + \epsilon^2 \eta^{(2)} + \epsilon^3 \eta^{(3)} \end{aligned}\right\} \quad (20)$$

where ϵ is an ordering parameter and the superscripts (1), (2) and (3) stand for the first-, second- and third-order solutions respectively.

In the following sections, a Stokes-type Fourier analysis is executed for the case of a flat bottom, where by substituting the above perturbation expansions into Eqs. (12)–(18) the first-, second- and third-order equations and the corresponding solutions are derived. The derived solutions are compared with the corresponding ones from Stokes wave theory in order to evaluate the model's linear and non-linear properties.

It should be mentioned that in SWASH model the application of a coarse vertical resolution combined with the Keller Box scheme for the discretisation of the pressure results to a poorer description of the vertical flow structure compared to the horizontal one. Consequently, the rather inaccurate vertical advective term of the vertical momentum equation, namely, the third term in Eqs. (17) and (18), is removed since this term can lead to instabilities or unrealistic results in some cases. Therefore, in the following derivations, the term $w_{r,12}w_{12}$ will be neglected.

3.1. First-order equations and solutions

After substituting the perturbation expansions into the governing equations of the two layer system (Eqs. (12)–(18)) and retaining only the of $O(\epsilon)$ terms, the first-order or linear equations are determined:

$$2\frac{\partial \eta^{(1)}}{\partial t} + d\frac{\partial u_{k1}^{(1)}}{\partial x} + d\frac{\partial u_{k2}^{(1)}}{\partial x} = 0 \quad (21)$$

$$d\frac{\partial u_{k2}^{(1)}}{\partial x} + 2w_s^{(1)} - 2w_{12}^{(1)} = 0 \quad (22)$$

$$d\frac{\partial u_{k1}^{(1)}}{\partial x} + 2w_{12}^{(1)} = 0 \quad (23)$$

$$2\frac{\partial u_{k2}^{(1)}}{\partial t} + 2g\frac{\partial \eta^{(1)}}{\partial x} + \frac{\partial q_{12}^{(1)}}{\partial x} = 0 \quad (24)$$

$$2\frac{\partial u_{k1}^{(1)}}{\partial t} + 2g\frac{\partial \eta^{(1)}}{\partial x} + \frac{\partial q_{12}^{(1)}}{\partial x} + \frac{\partial q_b^{(1)}}{\partial x} = 0 \quad (25)$$

$$d\frac{\partial w_s^{(1)}}{\partial t} + d\frac{\partial w_{12}^{(1)}}{\partial t} - 4q_{12}^{(1)} = 0 \quad (26)$$

$$d\frac{\partial w_{12}^{(1)}}{\partial t} + 4q_{12}^{(1)} - 4q_b^{(1)} = 0 \quad (27)$$

An important feature related to the applicability of phase-resolving wave models in deeper water conditions is whether they are efficient in accurately reproducing the linear (or frequency) dispersion. To derive the first-order solutions of the SWASH model, we consider a wave travelling along the x-direction with angular frequency ω and wave number k. The first-order solutions have the following form (Dingemans, 1997):

$$\left.\begin{aligned} u_{k1}^{(1)} &= u_{k1,01}\cos(kx-\omega t), & u_{k2}^{(1)} &= u_{k2,01}\cos(kx-\omega t), \\ w_s^{(1)} &= w_{s,01}\sin(kx-\omega t), & w_{12}^{(1)} &= w_{12,01}\sin(kx-\omega t), \\ q_{12}^{(1)} &= q_{12,01}\cos(kx-\omega t), & q_b^{(1)} &= q_{b,01}\cos(kx-\omega t), \\ \eta^{(1)} &= \eta_{01}\cos(kx-\omega t) \end{aligned}\right\} \quad (28)$$

Substituting the above solutions into Eqs. (21)–(27), the first-order solutions are obtained by solving the system of seven equations with seven unknowns. Here, the linear dispersion relation and the horizontal velocity components of the model in the case of two equidistant layers ($K = 2$) are presented:

$$\omega = \frac{4\sqrt{gk^2d\left(16+k^2d^2\right)}}{\sqrt{256+96k^2d^2+k^4d^4}} \quad (29)$$

$$u_{k1,01} = \frac{4\eta_{01}g\left(16-k^2d^2\right)}{\sqrt{gd\left(4096+1792k^2d^2+112k^4d^4+k^6d^6\right)}} \quad (30)$$

$$u_{k2,01} = \frac{4\eta_{01}g\left(16+3k^2d^2\right)}{\sqrt{gd\left(4096+1792k^2d^2+112k^4d^4+k^6d^6\right)}} \quad (31)$$

The derived solutions of layer-integrated horizontal velocity U ($U = \int_{z_k^-}^{z_k^+} u\,dz$), vertical velocity w and dynamic pressure p ($p = q + g\eta$) are normalised with respect to the theoretical solutions resulting from first-order Stokes wave theory (Dingemans, 1997) to determine the linear properties of the model. The ratios of U_{SW}/U_{St}, w_{SW}/w_{St} and p_{SW}/p_{St} are presented in Fig. 2, where the subscripts SW and St stand for SWASH and Stokes solutions, respectively. It is observed that the accuracy of the derived solutions for each layer, when compared to the theoretical solutions, increases with the number of layers. Additionally, in all cases the deviation between SWASH solutions and Stokes theory increases with the distance from the water surface.

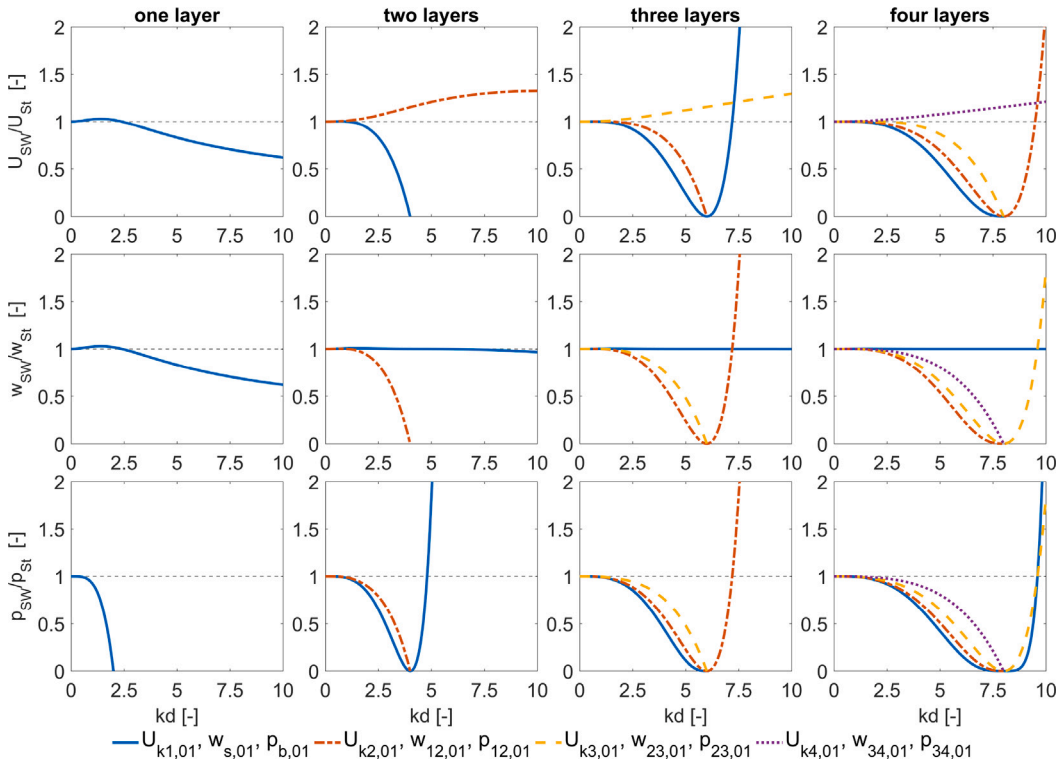

Fig. 2. Layer-dependent normalised first-order model solutions as a function of the number of vertical layers and dimensionless depth kd.

In Fig. 3, the normalised dispersion ω_{SW}/ω_{St} and the dynamic pressure at the bottom $p_{b,01SW}/p_{b,01St}$ are shown for a different number of layers. The normalised solutions of depth-integrated horizontal velocity $U_{t,01SW}/U_{t,01St}$ ($U_t = \int_{-d}^{0} u\mathrm{d}z$) and the vertical velocity at the surface $w_{s,01SW}/w_{s,01St}$ could also be compared for the different layer layouts. However, for a first-order analysis these solutions would coincide with the corresponding one for the normalised dispersion due to the linear free surface and continuity equations (Eqs. (21)–(23)). Fig. 3 shows that the accuracy of the model with respect to both linear dispersion and dynamic pressure significantly improves with an increasing number of layers over an extended range of kd values and, thus, up to very deep water. Increasing the number of layers corresponds to higher-order Padé approximants of the solutions in Eqs. (29)–(31) and, therefore, to an increased accuracy with respect to theoretical solutions. This procedure is equivalent to the inclusion of higher-order dispersive terms in Bossiness-type equations, also resulting to improved linear properties (Madsen and Schäffer, 1998).

Table 1 provides a summary of the ranges of dimensionless depth kd over which the error of the first-order wave parameters ω, U, w and p stays below 1% and 3%, respectively. For each parameter, the layer dependent solution with the highest deviation from the theoretical value has been used to define the kd range. It is observed that the use of a few vertical layers significantly improves the description of wave linear dispersion, even for deep water waves ($kd > \pi$). More precisely, the relative error for two layers is lower than 1% for kd values up to 7.71, while the corresponding threshold value for four layers increases to 28.59. On the other hand, the range of kd values over which the velocities and the dynamic pressure are accurately described by the model is much more limited.

3.2. Second-order equations and solutions

In addition to the correct representation of the linear dispersion relation, the non-linear properties of a wave model are also important. As the waves propagate to water of decreasing depth, their profile deviates from the sinusoidal solution of linear theory and becomes asymmetrical, with steeper crests and flatter troughs. The capability of the model to accurately describe this behaviour is directly related to its non-linear properties.

Table 1
Range of dimensionless depth kd as a function of the number of vertical layers and the corresponding relative error in the first-order wave parameters ω, U, w and p.

Number of layers	Range of dimensionless depth [–]				Error [%]
	ω	U_{01}	w_{01}	p_{01}	
1	$kd \leq 0.53$	$kd \leq 0.53$	$kd \leq 0.53$	$kd \leq 0.60$	≤1%
1	$kd \leq 1.33$	$kd \leq 1.33$	$kd \leq 1.33$	$kd \leq 0.79$	≤3%
2	$kd \leq 7.71$	$kd \leq 1.01$	$kd \leq 1.36$	$kd \leq 0.87$	≤1%
2	$kd \leq 9.74$	$kd \leq 1.66$	$kd \leq 1.66$	$kd \leq 1.18$	≤3%
3	$kd \leq 16.41$	$kd \leq 1.36$	$kd \leq 1.52$	$kd \leq 1.10$	≤1%
3	$kd \leq 21.20$	$kd \leq 1.94$	$kd \leq 1.94$	$kd \leq 1.51$	≤3%
4	$kd \leq 28.59$	$kd \leq 1.69$	$kd \leq 1.70$	$kd \leq 1.30$	≤1%
4	$kd \leq 37.24$	$kd \leq 2.22$	$kd \leq 2.22$	$kd \leq 1.81$	≤3%

Substituting the perturbation expansions (Eq. (20)) into the governing equations (Eqs. (12)–(18)) and retaining only the $O(\epsilon^2)$ terms, one gets the second-order equations:

$$2\frac{\partial \eta^{(2)}}{\partial t} + d\frac{\partial u_{k1}^{(2)}}{\partial x} + d\frac{\partial u_{k2}^{(2)}}{\partial x} = -\eta^{(1)}\left(\frac{\partial u_{k1}^{(1)}}{\partial x} + \frac{\partial u_{k2}^{(1)}}{\partial x}\right) - (u_{k1}^{(1)} + u_{k2}^{(1)})\frac{\partial \eta^{(1)}}{\partial x} \quad (32)$$

$$2d\frac{\partial u_{k2}^{(2)}}{\partial x} + 4w_s^{(2)} - 4w_{12}^{(2)} = -2\eta^{(1)}\frac{\partial u_{k2}^{(1)}}{\partial x} + (u_{k2}^{(1)} - u_{k1}^{(1)})\frac{\partial \eta^{(1)}}{\partial x} \quad (33)$$

$$2d\frac{\partial u_{k1}^{(2)}}{\partial x} + 4w_{12}^{(2)} = -2\eta^{(1)}\frac{\partial u_{k1}^{(1)}}{\partial x} + (u_{k2}^{(1)} - u_{k1}^{(1)})\frac{\partial \eta^{(1)}}{\partial x} \quad (34)$$

$$\begin{aligned} 2d\frac{\partial u_{k2}^{(2)}}{\partial t} + 2dg\frac{\partial \eta^{(2)}}{\partial x} + d\frac{\partial q_{12}^{(2)}}{\partial x} &= -\eta^{(1)}\left(2g\frac{\partial \eta^{(1)}}{\partial x} + \frac{\partial q_{12}^{(1)}}{\partial x} + 2\frac{\partial u_{k2}^{(1)}}{\partial t}\right) \\ &\quad - 3q_{12}^{(1)}\frac{\partial \eta^{(1)}}{\partial x} - u_{k1}^{(1)}\left(\frac{\partial \eta^{(1)}}{\partial t} - 2w_{12}^{(1)}\right) \\ &\quad - u_{k2}^{(1)}\left(3\frac{\partial \eta^{(1)}}{\partial t} + 4d\frac{\partial u_{k2}^{(1)}}{\partial x} - 2w_{12}^{(1)}\right) \end{aligned} \quad (35)$$

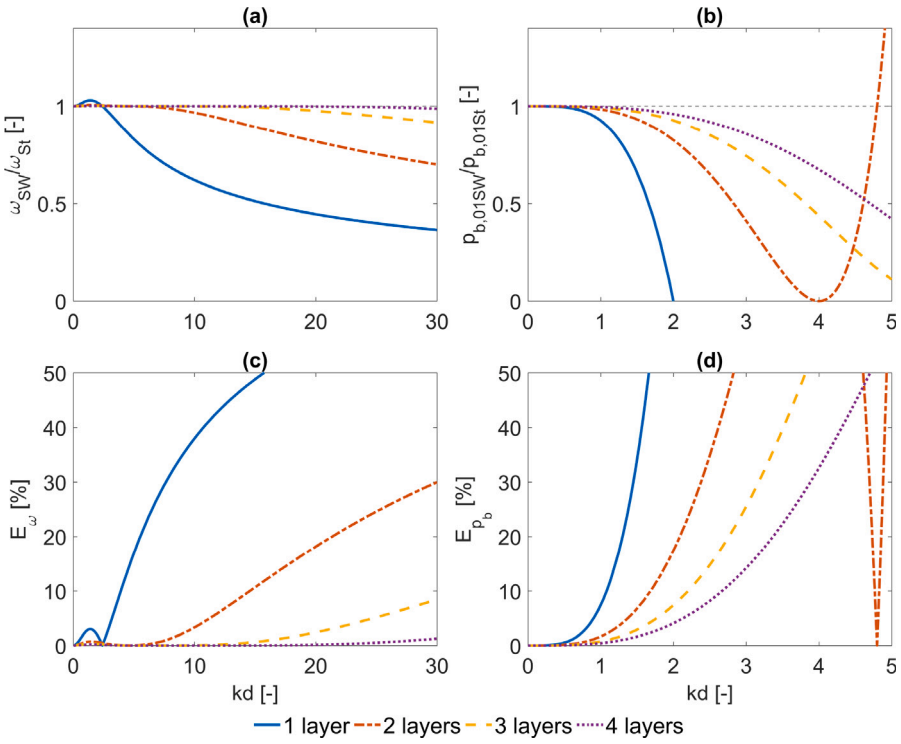

Fig. 3. Ratios and relative errors of first-order (a,c) dispersion ω_{SW}/ω_{St} and (b,d) dynamic pressure at the bottom $p_{b,01SW}/p_{b,01St}$ for one, two, three and four vertical layers as a function of the dimensionless depth kd.

$$
\begin{aligned}
&2d\frac{\partial u_{k1}^{(2)}}{\partial t}+2dg\frac{\partial \eta^{(2)}}{\partial x}+d\frac{\partial q_{12}^{(2)}}{\partial x}+d\frac{\partial q_b^{(2)}}{\partial x}\\
&\quad=-\eta^{(1)}\left(2g\frac{\partial \eta^{(1)}}{\partial x}+\frac{\partial q_{12}^{(1)}}{\partial x}+\frac{\partial q_b^{(1)}}{\partial x}+2\frac{\partial u_{k1}^{(1)}}{\partial t}\right)\\
&\quad-(q_b^{(1)}-q_{12}^{(1)})\frac{\partial \eta^{(1)}}{\partial x}+u_{k2}^{(1)}\left(\frac{\partial \eta^{(1)}}{\partial t}-2w_{12}^{(1)}\right)\\
&\quad-u_{k1}^{(1)}\left(\frac{\partial \eta^{(1)}}{\partial t}+4d\frac{\partial u_{k1}^{(1)}}{\partial x}+2w_{12}^{(1)}\right)
\end{aligned}
\tag{36}
$$

$$
\begin{aligned}
&d\frac{\partial w_s^{(2)}}{\partial t}+d\frac{\partial w_{12}^{(2)}}{\partial t}-4q_{12}^{(2)}=-du_{k2}^{(1)}\left(\frac{\partial w_{12}^{(1)}}{\partial x}+\frac{\partial w_s^{(1)}}{\partial x}\right)\\
&\quad-\eta^{(1)}\left(\frac{\partial w_{12}^{(1)}}{\partial t}+\frac{\partial w_s^{(1)}}{\partial t}\right)-w_{12}^{(1)}\left(d\frac{\partial u_{k2}^{(1)}}{\partial x}+\frac{\partial \eta^{(1)}}{\partial t}\right)\\
&\quad-w_s^{(1)}\left(d\frac{\partial u_{k2}^{(1)}}{\partial x}+\frac{\partial \eta^{(1)}}{\partial t}\right)
\end{aligned}
\tag{37}
$$

$$
d\frac{\partial w_{12}^{(2)}}{\partial t}+4q_{12}^{(2)}-4q_b^{(2)}=-du_{k1}^{(1)}\frac{\partial w_{12}^{(1)}}{\partial x}-\eta^{(1)}\frac{\partial w_{12}^{(1)}}{\partial t}-w_{12}^{(1)}\left(d\frac{\partial u_{k1}^{(1)}}{\partial x}+\frac{\partial \eta^{(1)}}{\partial t}\right)
\tag{38}
$$

As it is observed, the linear solutions provide forcing to the second-order solutions on the left hand side of Eqs. (32)–(38). More precisely, the linear solutions create self-interacting second-order harmonics which have the following form:

$$
\left.
\begin{aligned}
&u_{k1}^{(2)}=u_{k1,02}\cos(2kx-2\omega t), && u_{k2}^{(2)}=u_{k2,02}\cos(2kx-2\omega t),\\
&w_s^{(2)}=w_{s,02}\sin(2kx-2\omega t), && w_{12}^{(2)}=w_{12,02}\sin(2kx-2\omega t),\\
&q_{12}^{(2)}=q_{12,02}\cos(2kx-2\omega t), && q_b^{(2)}=q_{b,02}\cos(2kx-2\omega t),\\
&\eta^{(2)}=\eta_{02}\cos(2kx-2\omega t)
\end{aligned}
\right\}
\tag{39}
$$

Substituting the first (Eq. (28)) and second (Eq. (39)) order harmonics into the second-order equations and using the linear equations of Section 3.1, a system of fourteen equations ($2[3K+1]$) is obtained, from which the amplitudes of the second-order harmonics are derived in terms of kd and η_{01}. Here, the second-order amplitudes of the surface elevation, η_{02}, and of the horizontal velocities, $u_{k1,02}$ and $u_{k2,02}$, are presented for the case of two layers:

$$
\eta_{02}=\frac{\eta_{01}^2\left(49152+33792k^2d^2+9792k^4d^4+892k^6d^6+7k^8d^8\right)}{12k^2d^3\left(5120+640k^2d^2+36k^4d^4+k^6d^6\right)}
\tag{40}
$$

$$
u_{k1,02}=\frac{\eta_{01}^2 g\left(98304-43008k^2d^2+5760k^4d^4-904k^6d^6+37k^8d^8\right)}{6k^2d^3\left(320+20k^2d^2+k^4d^4\right)\sqrt{gd\left(4096+1792k^2d^2+112k^4d^4+k^6d^6\right)}}
\tag{41}
$$

$$
u_{k2,02}=\frac{\eta_{01}^2 g\left(98304+55296k^2d^2+18048k^4d^4+3608k^6d^6-33k^8d^8\right)}{6k^2d^3\left(320+20k^2d^2+k^4d^4\right)\sqrt{gd\left(4096+1792k^2d^2+112k^4d^4+k^6d^6\right)}}
\tag{42}
$$

The approximate expressions of surface elevation amplitude form $[6(K-1)+2, 6(K-1)]$ rational polynomials in terms of kd, which means that in the case of two layers we have an eighth-order and a sixth-order polynomial in the numerator and denominator respectively. The derived second-order amplitude expressions are compared with the theoretical solutions given by second-order Stokes wave theory (Dingemans, 1997) in order to study the second-order non-linear properties of the SWASH model as a function of the number of layers used.

It has to be mentioned that Taylor expansion has been applied in order to define the theoretical solutions at the same locations as in SWASH model. The ratios of U_{SW}/U_{St}, w_{SW}/w_{St} and p_{SW}/p_{St} are presented in Fig. 4. It is observed that when one vertical layer is employed then the model has poor representation of the second-order velocities and pressure both in shallow and deep water. However, as the number of layers increases the layer dependent second-order

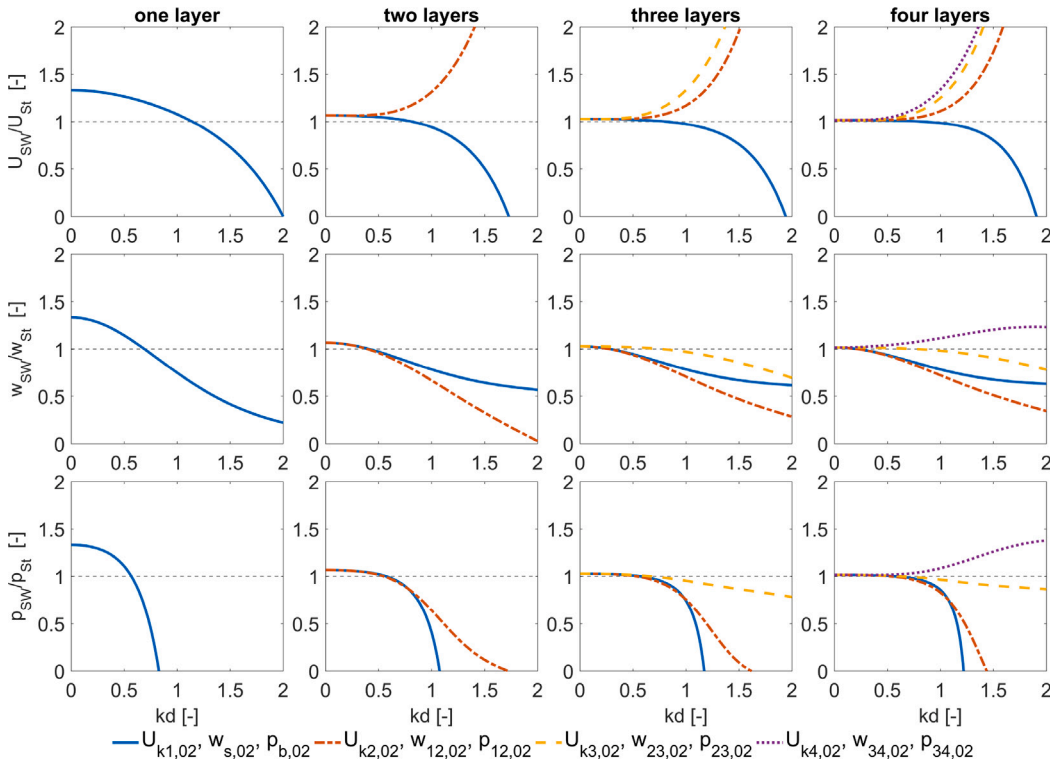

Fig. 4. Layer-dependent normalised second-order model solutions as a function of the number of vertical layers and dimensionless depth kd.

derived solutions agree with the theoretical ones over a larger range of dimensionless water depths.

In Fig. 5, the normalised second-order amplitudes of the surface elevation, η_{02SW}/η_{02St}, the depth-integrated horizontal velocity, $U_{t,02SW}/U_{t,02St}$, the vertical velocity at the surface $w_{s,02SW}/w_{s,02St}$ and the dynamic pressure at the bottom $p_{b,02SW}/p_{b,02St}$ for one, two, three and four vertical layers are presented as a function of the dimensionless depth kd. At the limit $kd \to 0$, the relative error of all non-linear parameters reduces from 33% to only 3% when shifting from one to three vertical layers, respectively.

Similar to what was witnessed in Section 3.1 regarding the linear properties, it can be verified here for the non-linear properties as well. The governing equations of the model, even when coarse vertical resolution is applied, can accurately reproduce the surface of a second-order wave over a large range of dimensionless depths in contrast with the velocities and dynamic pressure. More precisely, in case of four vertical layers the relative error in the second-order amplitude of the surface elevation stays below 10% up to a kd value of 4.36 while the corresponding value for the second-order amplitude of the horizontal velocities is only 0.69 (Table 2). Additionally, while the accuracy of the model improves as the number of layers increases for surface amplitude, vertical velocity, and dynamic pressure for all kd values, a divergence from the target solution is observed for large kd values in the second-order depth-integrated horizontal velocity with a finer vertical grid resolution.

3.3. Third-order solutions

Extending the Stokes-type Fourier analysis to the third-order, we seek for third-order harmonics of the form:

$$\left.\begin{aligned} u_{k1}^{(3)} &= u_{k1,03}\cos(3kx-3\omega t), & u_{k2}^{(3)} &= u_{k2,03}\cos(3kx-3\omega t),\\ w_{s}^{(3)} &= w_{s,03}\sin(3kx-3\omega t), & w_{12}^{(3)} &= w_{12,03}\sin(3kx-3\omega t),\\ q_{12}^{(3)} &= q_{12,03}\cos(3kx-3\omega t), & q_{b}^{(3)} &= q_{b,03}\cos(3kx-3\omega t),\\ \eta^{(3)} &= \eta_{03}\cos(3kx-3\omega t) \end{aligned}\right\} \tag{43}$$

However, at this order of analysis secular terms arise, introducing a non-uniformity in the expansion and resulting to unbounded in time solutions (Whitham, 1999). This issue can be addressed by expanding the first-order dispersion equation and harmonics in order to include third-order corrections in the first-order solutions (Madsen et al., 2003):

$$\left.\begin{aligned} u_{k1}^{(1)} &= u_{k1,01}(1+\epsilon^2 u_{k1,13})\cos(kx-\omega t), & u_{k2}^{(1)} &= u_{k2,01}(1+\epsilon^2 u_{k2,13})\cos(kx-\omega t),\\ w_{s}^{(1)} &= w_{s,01}(1+\epsilon^2 w_{s,13})\sin(kx-\omega t), & w_{12}^{(1)} &= w_{12,01}(1+\epsilon^2 w_{12,13})\sin(kx-\omega t),\\ q_{12}^{(1)} &= q_{12,01}(1+\epsilon^2 q_{12,13})\cos(kx-\omega t), & q_{b}^{(1)} &= q_{b,01}(1+\epsilon^2 q_{b,13})\cos(kx-\omega t),\\ \omega &= \omega_1(1+\epsilon^2\omega_{13}) \end{aligned}\right\} \tag{44}$$

where ω_{13} corresponds to the amplitude dispersion and terms with subscript "13" (x_{13}) represent the third-order correction to the first-order amplitudes. Substituting the perturbation expansions (Eq. (20)) into the governing equations (Eqs. (12)–(18)) and replacing the first (Eq. (44)), second (Eq. (39)) and third (Eq. (43)) order harmonics, the third-order solutions of the SWASH governing equations are derived by retaining only the $O(\epsilon^3)$ terms.

Here, we focus on the amplitude dispersion, ω_{13}, and the third-order component of the surface elevation, η_{03}, which using the Stokes wave theory are given by (Skjelbreia, 1959):

$$\omega_{13St} = \frac{1}{16}\eta_{01}^2 k^2 \frac{9\tanh^4(kd) - 10\tanh^2(kd) + 9}{\tanh^4(kd)} \tag{45}$$

$$\eta_{03St} = \frac{3}{64}\eta_{01}^3 k^2 \frac{1+8\cosh^6(kd)}{\sinh^6(kd)} \tag{46}$$

The amplitude dispersion and subsequently, the third-order component of the surface elevation are derived by eliminating the terms proportional to $\sin(kx-\omega t)$ and $\cos(kx-\omega t)$ from the third-order equations in order to remove secular unbounded solutions. In the case

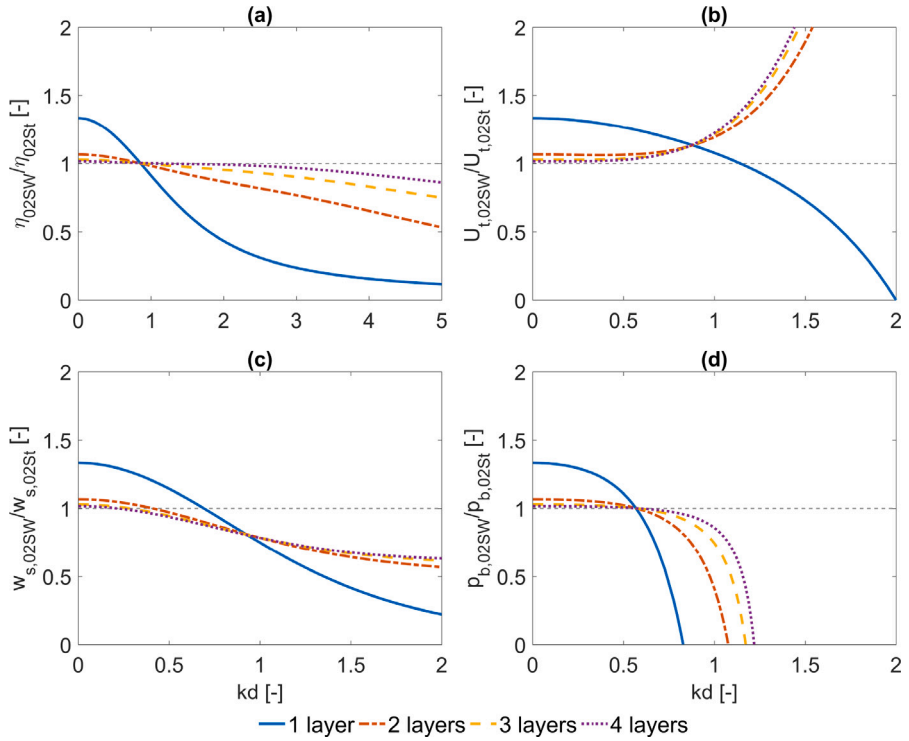

Fig. 5. Ratios of second-order (a) surface elevation η_{02SW}/η_{02St}, (b) depth-integrated horizontal velocity $U_{t,02SW}/U_{t,02St}$, (c) vertical velocity at the surface $w_{s,02SW}/w_{s,02St}$ and (d) dynamic pressure at the bottom $p_{b,02SW}/p_{b,02St}$ for one, two, three and four vertical layers as a function of the dimensionless depth kd.

Table 2
Range of dimensionless depth kd as a function of the number of vertical layers and the corresponding relative error in the second-order wave parameters η, U, w and p.

Number of layers	Range of dimensionless depth [–]				Error [%]
	η_{02}	U_{02}	w_{02}	p_{02}	
1	$0.78 \le kd \le 0.94$	$1.05 \le kd \le 1.22$	$0.63 \le kd \le 0.75$	$0.54 \le kd \le 0.59$	≤5%
1	$0.69 \le kd \le 1.02$	$0.96 \le kd \le 1.30$	$0.56 \le kd \le 0.81$	$0.51 \le kd \le 0.62$	≤10%
2	$0.40 \le kd \le 1.26$	–	$0.20 \le kd \le 0.52$	$0.35 \le kd \le 0.66$	≤5%
2	$kd \le 1.68$	$kd \le 0.62$	$kd \le 0.62$	$kd \le 0.74$	≤10%
3	$kd \le 2.09$	$kd \le 0.50$	$kd \le 0.46$	$kd \le 0.72$	≤5%
3	$kd \le 3.03$	$kd \le 0.68$	$kd \le 0.60$	$kd \le 0.82$	≤10%
4	$kd \le 3.41$	$kd \le 0.54$	$kd \le 0.44$	$kd \le 0.79$	≤5%
4	$kd \le 4.36$	$kd \le 0.69$	$kd \le 0.59$	$kd \le 0.90$	≤10%

of two layers the derived expressions are given by:

$$\begin{aligned}\omega_{13} =&\eta_{01}^2(1207959552 + 855638016k^2d^2 + 687341568k^4d^4\\ &+ 147062784k^6d^6 + 17270784k^8d^8 + 1173504k^{10}d^{10}\\ &+ 16568k^{12}d^{12} + 89k^{14}d^{14})/(96k^2d^4(16 + k^2d^2)^2\\ &(81920 + 35840k^2d^2 + 2496k^4d^4 + 116k^6d^6 + k^8d^8))\end{aligned} \tag{47}$$

$$\begin{aligned}\eta_{03} =&\eta_{01}^3(1207959552 + 1962934272k^2d^2 + 1738014720k^4d^4\\ &+ 682622976k^6d^6 + 145885184k^8d^8 + 14327296k^{10}d^{10}\\ &+ 267928k^{12}d^{12} + 2853k^{14}d^{14})/(384k^4d^6(16 + k^2d^2)\\ &(320 + 20k^2d^2 + k^4d^4)(1280 + 160k^2d^2 + 9k^4d^4))\end{aligned} \tag{48}$$

In Fig. 6, the normalised amplitude dispersion ($\omega_{13SW}/\omega_{13St}$) and the third-order amplitude of the surface elevation (η_{03SW}/η_{03St}) for one, two, three and four vertical layers are presented as a function of the dimensionless depth kd.

As observed from the figure, the model underestimates significantly the amplitude dispersion for kd values larger than 1, while increasing the number of layers improves the accuracy only in shallow water. On the other hand, the capability of the model to represent the third-order amplitude of the surface elevation increases considerably when more than two layers are applied, resulting to relative errors lower than 10% for kd values up to 1.85 and 3.04 for three and four layers, respectively. The results are summarised in Table 3.

Table 3
Range of dimensionless depth kd as a function of the number of vertical layers and the corresponding relative error in the amplitude dispersion ω_{13} and the third-order amplitude of the surface elevation η_{03}.

Number of layers	Range of dimensionless depth [–]		Error [%]
	ω_{13}	η_{03}	
1	$0.66 \le kd \le 0.76$	$0.68 \le kd \le 0.74$	≤5%
1	$0.61 \le kd \le 0.80$	$0.65 \le kd \le 0.78$	≤10%
2	$0.35 \le kd \le 0.68$	$0.55 \le kd \le 0.90$	≤5%
2	$kd \le 0.77$	$0.34 \le kd \le 1.07$	≤10%
3	$kd \le 0.66$	$0.24 \le kd \le 1.33$	≤5%
3	$kd \le 0.77$	$kd \le 1.85$	≤10%
4	$kd \le 0.65$	$kd \le 2.51$	≤5%
4	$kd \le 0.77$	$kd \le 3.04$	≤10%

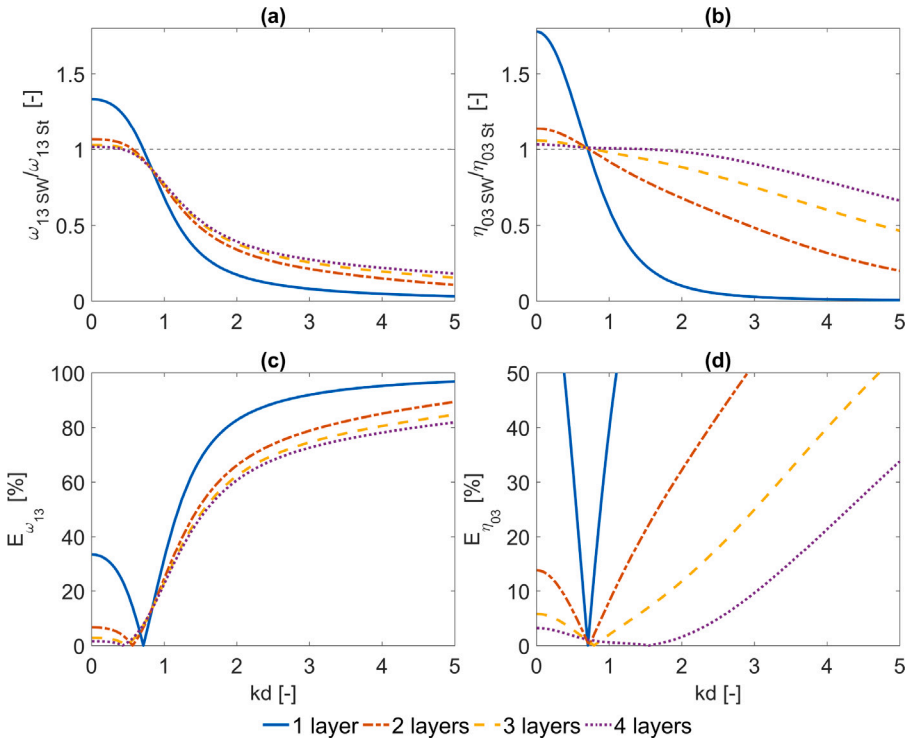

Fig. 6. Ratios and relative errors of (a,c) amplitude dispersion $\omega_{13SW}/\omega_{13St}$ and (b,d) third-order amplitude of the surface elevation η_{03SW}/η_{03St} for one, two, three and four vertical layers as a function of the dimensionless depth kd.

3.4. Transfer functions for second-order sub-harmonics and super-harmonics

In coastal regions, the principal non-linear processes are related to the near-resonant interactions among triads of waves. Waves with different frequencies interact with each other, leading to the generation of bound sub-harmonics and super-harmonics at the difference and sum of the frequencies of the primary waves. During this process substantial spectral energy is being transferred from the peak- to the low- and high-frequency part of the spectrum.

An important property of non-linear wave models refers to their efficiency to accurately describe the above-mentioned wave-wave interactions. Hence, an investigation of the efficiency of the SWASH model in reproducing second-order interactions is presented in the following. A first-order wave group composed of two harmonics with frequencies ω_m and ω_n and wave numbers k_m and k_n, respectively, is described as follows in the case of two layers:

$$\left.\begin{aligned} u_{k1}^{(1)} &= u_{k1,01m}\cos\vartheta_m + u_{k1,01n}\cos\vartheta_n, \quad u_{k2}^{(1)} = u_{k2,01m}\cos\vartheta_m + u_{k2,01n}\cos\vartheta_n,\\ w_s^{(1)} &= w_{s,01m}\sin\vartheta_m + w_{s,01n}\sin\vartheta_n, \quad w_{12}^{(1)} = w_{12,01m}\sin\vartheta_m + w_{12,01n}\sin\vartheta_n,\\ q_{12}^{(1)} &= q_{12,01m}\cos\vartheta_m + q_{12,01n}\cos\vartheta_n, \quad q_b^{(1)} = q_{b,01m}\cos\vartheta_m + q_{b,01n}\cos\vartheta_n,\\ \eta^{(1)} &= \eta_{01m}\cos\vartheta_m + \eta_{01n}\cos\vartheta_n \end{aligned}\right\} \tag{49}$$

where $\vartheta_m = k_m x - \omega_m t$ and $\vartheta_n = k_n x - \omega_n t$.

In the above first-order wave group, both harmonics are considered solutions of the linearised governing equations (Eqs. (21)–(27)) and subsequently frequencies ω_m and ω_n satisfy the linear dispersion relation derived in Section 3.1 (Eq. (29)). Through the non-linear terms a first-order bichromatic wave group will force a second-order wave group composed of four components, one sub-harmonic, $\omega_m - \omega_n$, and three super-harmonics, $2\omega_m$, $2\omega_n$ and $\omega_m + \omega_n$. These components are bound (phase locked) to the first-order wave group, while frequencies $\omega_m - \omega_n$, $2\omega_m$, $2\omega_n$ and $\omega_m + \omega_n$ do not satisfy the linear dispersion relation. The second-order wave group is described as follows in the case of two layers:

$$\left.\begin{aligned} u_{k1}^{(2)} &= G_{u_{k1}}^{m-n}\cos(\vartheta_m - \vartheta_n) + G_{u_{k1}}^{2m}\cos(2\vartheta_m) + G_{u_{k1}}^{m+n}\cos(\vartheta_m + \vartheta_n) + G_{u_{k1}}^{2n}\cos(2\vartheta_n)\\ u_{k2}^{(2)} &= G_{u_{k2}}^{m-n}\cos(\vartheta_m - \vartheta_n) + G_{u_{k2}}^{2m}\cos(2\vartheta_m) + G_{u_{k2}}^{m+n}\cos(\vartheta_m + \vartheta_n) + G_{u_{k2}}^{2n}\cos(2\vartheta_n)\\ w_s^{(2)} &= G_{w_s}^{m-n}\sin(\vartheta_m - \vartheta_n) + G_{w_s}^{2m}\sin(2\vartheta_m) + G_{w_s}^{m+n}\sin(\vartheta_m + \vartheta_n) + G_{w_s}^{2n}\sin(2\vartheta_n)\\ w_{12}^{(2)} &= G_{w_{12}}^{m-n}\sin(\vartheta_m - \vartheta_n) + G_{w_{12}}^{2m}\sin(2\vartheta_m) + G_{w_{12}}^{m+n}\sin(\vartheta_m + \vartheta_n) + G_{w_{12}}^{2n}\sin(2\vartheta_n)\\ q_{12}^{(2)} &= G_{q_{12}}^{m-n}\cos(\vartheta_m - \vartheta_n) + G_{q_{12}}^{2m}\cos(2\vartheta_m) + G_{q_{12}}^{m+n}\cos(\vartheta_m + \vartheta_n) + G_{q_{12}}^{2n}\cos(2\vartheta_n)\\ q_b^{(2)} b &= G_{q_b}^{m-n}\cos(\vartheta_m - \vartheta_n) + G_{q_b}^{2m}\cos(2\vartheta_m) + G_{q_b}^{m+n}\cos(\vartheta_m + \vartheta_n) + G_{q_b}^{2n}\cos(2\vartheta_n)\\ \eta^{(2)} &= G_{\eta}^{m-n}\cos(\vartheta_m - \vartheta_n) + G_{\eta}^{2m}\cos(2\vartheta_m) + G_{\eta}^{m+n}\cos(\vartheta_m + \vartheta_n) + G_{\eta}^{2n}\cos(2\vartheta_n) \end{aligned}\right\} \tag{50}$$

where G^{m-n} is the sub-harmonic transfer function, G^{2m}, G^{2n} and G^{m+n} are the super-harmonic transfer functions.

Substituting the first (Eq. (49)) and second (Eq. (50)) order wave groups into the second-order equations (Eqs. (32)–(38)), the second-order transfer functions are derived in terms of $k_m d$, $k_n d$, ω_m, ω_n, η_{01m} and η_{01n}. Here, the second-order transfer functions of the surface elevation, G_η^{m-n} and G_η^{m+n} in the case of two layers are presented:

$$\begin{aligned} G_\eta^{m-n} =& \eta_{01m}\eta_{01n}(k_m - k_n)^2(65536\omega_m\omega_n(k_n^2\omega_m^2 + 4k_m k_n\omega_m\omega_n + k_m^2\omega_n^2)\\ &- 65536 g k_m k_n d(2k_n^2\omega_m^2 + k_m k_n\omega_m\omega_n + 2k_m^2\omega_n^2) + k_m^3(k_m - k_n)^2\\ &k_n^3 d^8\omega_m\omega_n(-k_n(k_m + 4k_n)\omega_m^2 + 2(k_m^2 + 3k_m k_n + k_n^2)\omega_m\omega_n\\ &- k_m(4k_m + k_n)\omega_n^2) + 4096 g k_m k_n d^3(-k_n^2(-4k_m^2 + 8k_m k_n + k_n^2)\omega_m^2\\ &+ 6k_m(k_m - k_n)^2 k_n\omega_m\omega_n - k_m^2(k_m^2 + 8k_m k_n - 4k_n^2)\omega_n^2)\\ &+ 256 g k_m k_n d^5(k_n^2(-10k_m^4 + 4k_m^3 k_n + 10k_m^2 k_n^2 - 6k_m k_n^3 + k_n^4)\omega_m^2\\ &- k_m k_n(k_m^4 + k_m^3 k_n - 5k_m^2 k_n^2 + k_m k_n^3 + k_n^4)\omega_m\omega_n + k_m^2(k_m^4 - 6k_m^3 k_n\\ &+ 10k_m^2 k_n^2 + 4k_m k_n^3 - 10k_n^4)\omega_n^2) + 16 g k_m^3(k_m - k_n)^2 k_n^3 d^7\\ &(k_n^2\omega_m(3\omega_m + \omega_n) + k_m^2\omega_n(\omega_m + 3\omega_n) - k_m k_n(4\omega_m^2 + 5\omega_m\omega_n + 4\omega_n^2))\\ &+ 4096 d^2(32 g^2 k_m^3 k_n^3 + \omega_m\omega_n(-2k_n^4\omega_m^2 + 6k_m^3 k_n\omega_m\omega_n - 2k_m^4\omega_n^2\\ &+ 6k_m k_n^3\omega_m\omega_n + k_m^2 k_n^2(-9\omega_m^2 + 14\omega_m\omega_n - 9\omega_n^2))) + 16 k_m k_n d^6 \end{aligned}$$

$$(-16g^2k_m^2(k_m-k_n)^4k_n^2+\omega_m\omega_n(-2k_m^6\omega_m\omega_n-2k_n^6\omega_m\omega_n+k_mk_n^5(2\omega_m+\omega_n)(12\omega_m+\omega_n)+k_m^5k_n(\omega_m+2\omega_n)(\omega_m+12\omega_n)+2k_m^4k_n^2(\omega_m^2+2\omega_m\omega_n-21\omega_n^2)+2k_m^3k_n^3(\omega_m^2-3\omega_m\omega_n+\omega_n^2)+2k_m^2k_n^4(-21\omega_m^2+2\omega_m\omega_n+\omega_n^2)))+256d^4(16g^2k_m^3(k_m-k_n)^2k_n^3+\omega_m\omega_n(k_n^6\omega_m^2+k_m^6\omega_n^2+k_m^4k_n^2(-9\omega_m^2+28\omega_m\omega_n-15\omega_n^2)+k_m^2k_n^4(-15\omega_m^2+28\omega_m\omega_n-9\omega_n^2)+2k_m^3k_n^3(23\omega_m^2-40\omega_m\omega_n+23\omega_n^2))))/(2k_m^2k_n^2d(-16+k_m^2d^2)(-16+k_n^2d^2)\omega_m(-256g(k_m-k_n)^2d-16g(k_m-k_n)^4d^3+256(\omega_m-\omega_n)^2+96(k_m-k_n)^2d^2(\omega_m-\omega_n)^2+(k_m-k_n)^4d^4(\omega_m-\omega_n)^2)\omega_n) \quad (51)$$

$$G_\eta^{m+n}=\eta_{01m}\eta_{01n}(k_m+k_n)^2(65536\omega_m\omega_n(k_n^2\omega_m^2+4k_mk_n\omega_m\omega_n+k_m^2\omega_n^2)-65536gk_mk_nd(2k_n^2\omega_m^2+k_mk_n\omega_m\omega_n+2k_m^2\omega_n^2)+4096gk_mk_nd^3(k_n^2(4k_m^2+8k_mk_n-k_n^2)\omega_m^2+6k_mk_n(k_m+k_n)^2\omega_m\omega_n+k_m^2(-k_m^2+8k_mk_n+4k_n^2)\omega_n^2)-16gk_m^3k_n^3(k_m+k_n)^2d^7(k_n^2(\omega_m-3\omega_n)\omega_n+k_n^2\omega_m(-3\omega_m+\omega_n)+k_mk_n(-4\omega_m^2+5\omega_m\omega_n-4\omega_n^2))+k_m^3k_n^3(k_m+k_n)^2d^8\omega_m\omega_n(2k_n^2\omega_m(2\omega_m+\omega_n)+2k_m^2\omega_n(\omega_m+2\omega_n)-k_mk_n(\omega_m^2+6\omega_m\omega_n+\omega_n^2))+256gk_mk_nd^5(k_n^6\omega_m^2+k_mk_n^5\omega_m(6\omega_m-\omega_n)+k_m^6\omega_n^2+k_m^5k_n\omega_n(-\omega_m+6\omega_n)+k_m^2k_n^4(10\omega_m^2+\omega_m\omega_n-10\omega_n^2)+k_m^3k_n^3(-4\omega_m^2+5\omega_m\omega_n-4\omega_n^2)+k_m^4k_n^2(-10\omega_m^2+\omega_m\omega_n+10\omega_n^2))+16k_mk_nd^6(-16g^2k_m^2k_n^2(k_m+k_n)^4+\omega_m\omega_n(k_m^5k_n(\omega_m-12\omega_n)(\omega_m-2\omega_n)-2k_m^6\omega_m\omega_n-2k_n^6\omega_m\omega_n-2k_m^4k_n^2(\omega_m^2-2\omega_m\omega_n-21\omega_n^2)+2k_m^2k_n^4(21\omega_m^2+2\omega_m\omega_n-\omega_n^2)+k_mk_n^5(24\omega_m^2-14\omega_m\omega_n+\omega_n^2)+2k_m^3k_n^3(\omega_m^2+3\omega_m\omega_n+\omega_n^2)))+4096d^2(32g^2k_m^3k_n^3+\omega_m\omega_n(-2k_n^4\omega_m^2+6k_m^3k_n\omega_m\omega_n+6k_mk_n^3\omega_m\omega_n-2k_m^4\omega_n^2-k_m^2k_n^2(9\omega_m^2+14\omega_m\omega_n+9\omega_n^2)))+256d^4(16g^2k_m^3k_n^3(k_m+k_n)^2+\omega_m\omega_n(k_n^6\omega_m^2+k_m^6\omega_n^2-k_m^2k_n^4(15\omega_m^2+28\omega_m\omega_n+9\omega_n^2)-k_m^4k_n^2(9\omega_m^2+28\omega_m\omega_n+15\omega_n^2)-2k_m^3k_n^3(23\omega_m^2+40\omega_m\omega_n+23\omega_n^2))))/(2k_m^2k_n^2d(-16+k_m^2d^2)(-16+k_n^2d^2)\omega_m\omega_n(-256g(k_m+k_n)^2d-16g(k_m+k_n)^4d^3+256(\omega_m+\omega_n)^2+96(k_m+k_n)^2d^2(\omega_m+\omega_n)^2+(k_m+k_n)^4d^4(\omega_m+\omega_n)^2)) \quad (52)$$

Similar expressions can be derived for the transfer functions of velocity and non-hydrostatic pressure components but they are not shown here. The self interacting super-harmonic transfer functions, G_η^{2m} and G_η^{2n}, are the same as the second-order solution derived and analysed in Section 3.2. By substituting the linear dispersion relation (Eq. (29)) for ω_m and ω_n in the above expressions, the derived transfer functions can be compared with the reference solutions for the sub- and super-harmonics given by Schäffer (1996) and Sand and Mansard (1986), respectively. Their second-order solutions are derived from the non-linear boundary value problem for the Laplace equation using a perturbation method.

In Fig. 7 the normalised sub-harmonic and super-harmonic transfer functions $G_{\eta,SW}^{m\pm n}/G_{\eta,th}^{m\pm n}$ for one, two, three and four vertical layers are presented as a function of the dimensionless depths k_md and k_nd. The normalised sub-harmonic and super-harmonic are located below and above diagonal respectively, while the green colour represents the area where the relative error is less than 10%.

Regarding the sub-harmonic transfer function, the model's agreement with the theoretical solution improves significantly when two layers are used instead of one. Further increasing the number of layers enhances the model's properties in the low kd range, where the error reduces below 5%. In general, for a multi-layer layout the governing equations are capable of accounting for second-order interactions between shallow water waves (e.g. $k_md \leq 0.7$) and intermediate-deep water waves (e.g. $k_nd \geq 1.0$). However, for second-order interactions between intermediate and deep water waves (k_nd, $k_md \geq 1.8$) the error is larger than 10%. Fortunately, the energy transfer to sub-harmonics is pronounced in shallow water, where the transfer functions are also more accurately described by the model. The limit case of $k_nd \to k_md$ (on the diagonal) corresponds to the solution for the wave set-down under a wave group, which can be described by the model with an error lower than 10% for kd values up to 1.8.

Table 4
Index of agreement of the second-order sub-harmonic and super-harmonic transfer functions of the surface elevation amplitude.

Number of layers	Index of agreement $\kappa_m'=\kappa_n'=3$	Index of agreement $\kappa_m'=\kappa_n'=5$
1	0.663	0.403
2	0.895	0.760
3	0.919	0.805
4	0.924	0.818

Regarding the super-harmonic transfer function, the agreement with the theoretical expression in the case of one layer is better than what was observed with the sub-harmonic transfer function. The combinations of k_md and k_nd for which the error is less than 10% (green area) increase remarkably with the number of layers and consequently for three and four layers the model is capable of accounting even for second-order interactions between intermediate and deep water waves. In this case, the diagonal where $k_nd = k_md$ corresponds to the self interacting super-harmonic transfer functions, G_η^{2m} and G_η^{2n}, and thus the values are the same as the ones corresponding to the normalised second-order amplitude of the surface elevation, η_{02SW}/η_{02St}, presented in Fig. 5a.

Additionally, in Fig. 8 the normalised sub-harmonic and super-harmonic transfer functions of the depth-integrated horizontal velocities $G_{U,SW}^{m\pm n}/G_{U,th}^{m\pm n}$ in the case of two vertical layers are showed as a function of the dimensionless depths k_md and k_nd. Here, in contrast to the transfer functions of the surface elevation amplitude, the combinations of k_md and k_nd for which the model reproduces accurately the transfer functions of the horizontal velocities is much more limited. The deviation from the theoretical solution is larger for the second layer near the surface compared to the first layer near the bottom, while the relative error stays below 20% (green area) in both layers up to k_md and k_nd values of 0.85.

Moreover, the derived second-order sub-harmonic and super-harmonic transfer functions of the surface elevation amplitude are evaluated using the following index of agreement (Kennedy et al., 2001):

$$IA = 1 - \sqrt{\frac{1}{2\kappa_m'\kappa_n'}\int_0^{\kappa_m'}\int_0^{\kappa_n'}\left(\frac{G_{SW}^{m+n}}{G_{th}^{m+n}}-1\right)^2+\left(\frac{G_{SW}^{m-n}}{G_{th}^{m-n}}-1\right)^2 d(\kappa_m)d(\kappa_n)} \quad (53)$$

where $\kappa_m = k_md$ and $\kappa_n = k_nd$, while the model is evaluated for two cases: (a) $\kappa_m' = \kappa_n' = 3$ and (b) $\kappa_m' = \kappa_n' = 5$. An IA value of 1 indicates a perfect agreement with the theoretical transfer functions. The results are summarised in Table 4, where it is noticed that the index of agreement increases from 0.663 for one layer to 0.924 for four layers for the first case and from 0.403 for one layer to 0.818 for four layers for the second case.

4. Wave generation and absorption using derived solutions

In the previous section the linear and non-linear solutions of the non-hydrostatic governing equations have been derived when one, two, three and four vertical layers are employed. These derived expressions can be used to formulate improved wave generation and absorption boundary conditions for non-hydrostatic models. In SWASH model there are two methods to generate waves, the weakly reflective wave generation method where the waves are generated at the boundary of

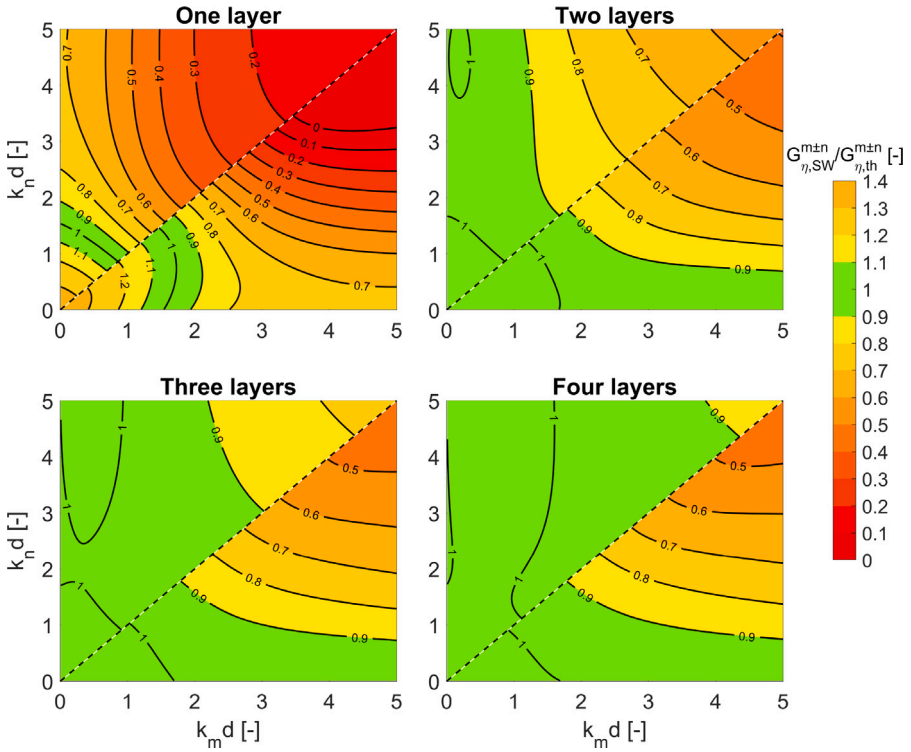

Fig. 7. Normalised sub-harmonic (below diagonal) and super-harmonic (above diagonal) transfer functions $G^{m\pm n}_{\eta,SW}/G^{m\pm n}_{\eta,th}$ for one, two, three and four vertical layers as a function of the dimensionless depths $k_m d$ and $k_n d$.

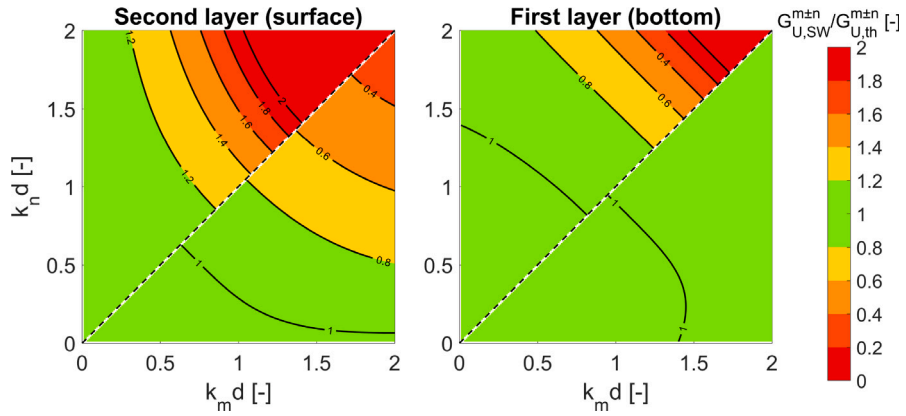

Fig. 8. Normalised sub-harmonic (below diagonal) and super-harmonic (above diagonal) transfer functions of the depth-integrated horizontal velocities $G^{m\pm n}_{U,SW}/G^{m\pm n}_{U,th}$ in the case of two vertical layers as a function of the dimensionless depths $k_m d$ and $k_n d$.

the computational domain and the internal wave generation method where the waves are generated inside the computational domain over an area called source area (Vasarmidis et al., 2019, 2021). Here we will apply the derived solutions in the former method but the application in the latter one is also straightforward.

According to the weakly reflective wave generation method, waves are generated by imposing the horizontal velocities of the incident waves in each layer over the vertical direction of the computational boundary. Additionally, in order to absorb the reflected waves that are propagating towards the generation boundary and to prevent re-reflections a radiation condition is applied at the same location in each layer. As a result the imposed horizontal velocity for layer k ($z_{k^-} \leq z \leq z_{k^+}$) is given by (Blayo and Debreu, 2005):

$$u_k = u_{k,t} + \frac{c_0}{d}(\eta_t - \eta_i) \tag{54}$$

where c_0 is the local wave speed, $u_{k,t}$ is the target horizontal velocity for layer k, η_t is the target surface elevation and η_i is the instantaneous surface elevation computed at the cell next to the boundary. The value of c_0 should be decided a priori by the user and in case that the reflected wave approaches the wave generation boundary with a speed of $c = c_0$, then the wave will be perfectly absorbed at the location of the boundary (Higdon, 1987). In most nearshore applications it is assumed that the reflected waves propagate with the shallow water wave speed ($c_0 = \sqrt{gd}$), which is independent of the wave number, since in coastal areas the short waves (high-frequency energy) are dissipated near the shoreline while long waves (low-frequency energy) are reflected back.

Table 5
Summary of wave conditions of the under examination cases.

Wave conditions	Wave height [m]		Wave period [s]		Dimensionless depth [–]	
1st order monochromatic	$H = 0.05$		$T = 5.0$		$kd = 4.02$	
1st order monochromatic	$H = 0.05$		$T = 4.1$		$kd = 5.98$	
2nd order monochromatic	$H = 0.80$		$T = 12.0$		$kd = 0.55$	
2nd order monochromatic	$H = 1.20$		$T = 7.0$		$kd = 1.05$	
2nd order bichromatic	$H_m = 0.60$	$H_n = 0.80$	$T_m = 10.0$	$T_n = 12.0$	$kd_m = 0.68$	$kd_n = 0.55$
2nd order bichromatic	$H_m = 1.00$	$H_n = 1.20$	$T_m = 6.5$	$T_n = 7.0$	$kd_m = 1.16$	$kd_n = 1.05$

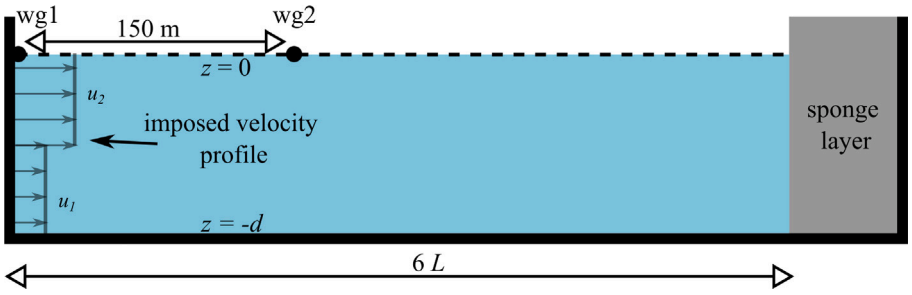

Fig. 9. Definition sketch of the implemented set-up for the numerical simulations, where L represents the wave length of each examined case.

In the above formulation (Eq. (54)), the imposed target horizontal velocity components, $u_{k,t}$, for each layer can be defined using the derived linear and non-linear velocity amplitudes. Additionally, the corresponding surface elevation amplitude that has also been derived can be used as the target surface elevation η_t. In this way, any difference between the target surface elevation, η_t, and the instantaneous surface elevation, η_i, is taken as reflection and thus it is absorbed at the generation boundary of the computational domain.

To demonstrate the ability of the SWASH model to generate accurately linear and non-linear waves using the derived solutions, first- and second-order monochromatic waves and second-order bichromatic waves are examined in the following sections. The cases under consideration are summarised in Table 5 and were categorised based on Le Méhauté's diagram (Méhauté, 1976). The numerical flume used for all the following cases is presented in Fig. 9, with a weakly reflective wave generator positioned at the left boundary and a sponge layer at the right boundary.

4.1. First-order monochromatic waves

At first, we consider two test cases of first-order monochromatic waves (Table 5) with a wave height $H = 0.05$ m, a water depth of $d = 25$ m and two different wave periods T of 5 s and 4.1 s. The resulting dimensionless depths kd of these highly dispersive waves are 4.02 and 5.98 and thus two vertical layers are applied in order to keep the relative error in wave dispersion below 1% (Table 1). For both cases, the grid cell size Δx is determined by the condition of having at least 50 grid cells per wave length, resulting in values of $\Delta x = 0.5$ m and $\Delta x = 0.3$ m for the first and second cases, respectively. Furthermore, an automatic time step control is used throughout the simulations, following the CFL (Courant–Friedrichs–Lewy) condition. According to this criterion, the time step is reduced by half when the Courant number exceeds a specified maximum value, and it is doubled when the Courant number falls below a specified minimum value. For this study, a maximum CFL value of 0.5 and a minimum CFL value of 0.2 are applied in all simulations.

In SWASH, in case of a multi-layer layout of the model, the target horizontal velocity component in the formulation of the weakly reflective wave generation boundary (Eq. (54)) is described by default by a hyperbolic cosine profile, and the theoretical velocities resulting from first-order Stokes (Airy) wave theory are imposed. However, since now the exact solutions of the governing equations have been defined, the derived expressions as discussed in Section 3 can be implemented in the code. In Fig. 10, the normalised surface elevation η/α_0 and wave height H/H_0 are presented for both wave conditions, where H_0 is the target wave height and $\alpha_0 = H_0/2$. The waves are generated at the boundary of the computational domain by imposing the theoretical solutions (blue dashed lines) and by imposing the linear derived solutions (red dashed lines) of Section 3.1 (Eqs. (29)–(31)).

As it is observed, when the theoretical solutions are used as the target horizontal velocity $u_{k,t}$ (Eq. (54)) at the boundary, a sharp decrease of the surface elevation amplitude and consequently of the wave height is noticed at the first computational cells next to the wave generation boundary, leading to a bad agreement with the target profile. This is a well-known deficiency of the model (Vasarmidis et al., 2021), and the deviation of the generated surface elevation from the target one is becoming larger for higher values of dimensionless depth. More precisely, in the case of $kd = 4.02$ the resulting wave height is 9% smaller than the target one, while for $kd = 5.98$ the percentage difference increases to 15%.

This deficiency can be explained by Fig. 2, where it can be noticed that in the case of two layers and kd values larger than 2.5, the derived solutions of the layer-integrated horizontal velocities U deviate significantly from the theoretical ones, and for $kd \geq 4.0$ even a reverse flow is observed at the bottom layer. As a result, since the imposed theoretical solutions do not verify the system of the linearised governing equations (Eqs. (21)–(27)), these solutions are transformed at the first cells as they propagate inside the computational domain leading to a decrease in the surface elevation amplitude. In addition, the transformation of the surface elevation affects the computed instantaneous surface elevation η_i at the cell next to the generation boundary which differs from the target one η_t. Subsequently, the imposed radiation condition at the boundary considers this difference as a reflected wave and tries to absorb it, leading to further disturbance of the generated wave profile.

A common technique to overcome this deficiency is calibration by using a larger wave height as an input. However, this calibration procedure to achieve the target wave height inside the computational domain is becoming even more difficult in the case of irregular waves

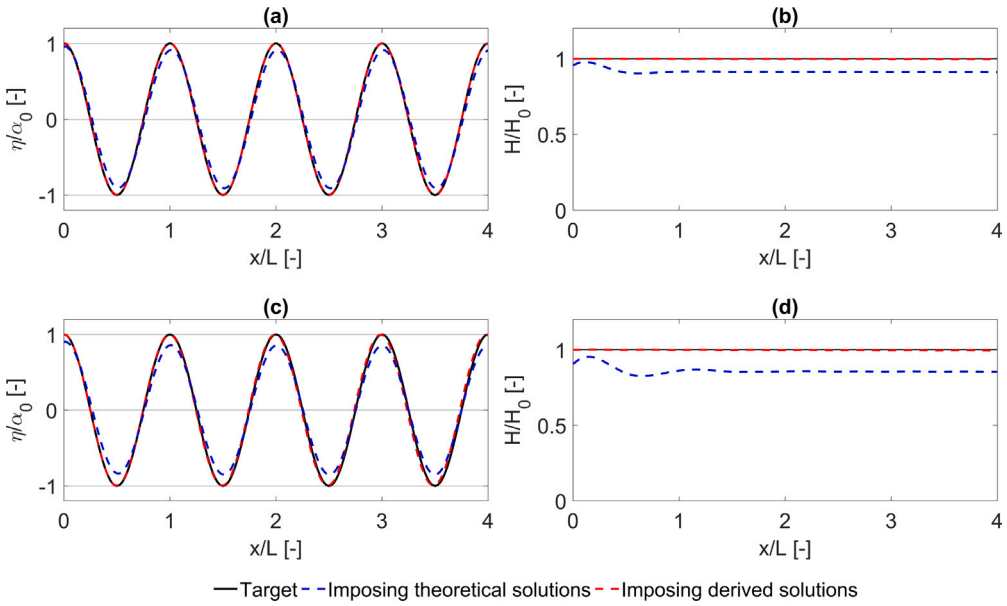

Fig. 10. Comparison between computed (dashed lines) and target (solid lines) normalised surface elevation η/α_0 and wave height H/H_0 for the case of linear waves with dimensionless depth (a, (b) $kd = 4.02$ and (c, (d) $kd = 5.98$. The waves are generated at the boundary of the computational domain by imposing the theoretical solutions (blue dashed lines) and the derived solutions (red dashed lines).

since, as it is also witnessed here, the sharp decrease of the surface elevation amplitude is different for each kd value and hence for each frequency. So in case of irregular waves, imposing a larger significant wave height as an input leads to an overestimation of the low frequency energy (small kd values) due to the fact that the velocities of the model in this range of frequencies agree well with the theoretical ones.

On the other hand, by using the first-order derived solutions as an input at the weakly reflective wave generation boundary, we avoid the problem of the sharp decrease of the surface elevation and thus the need of calibration. As it is shown in Fig. 10, the computed surface elevation and wave height have an excellent agreement with the target values all over the computational domain of four wave lengths. Furthermore, it has to be mentioned that using three or four layers with the corresponding derived velocity expressions as input results in identical profiles. This excellent agreement indicates that the derived solutions can be used to significantly improve the capability of the model to accurately generate linear waves at any depth. The same conclusion holds valid for any non-hydrostatic wave model.

4.2. Second-order monochromatic and bichromatic waves

In this section, the capability of the model to generate accurately second-order monochromatic and bichromatic waves using the derived solutions is examined. Two different second-order monochromatic waves are considered. The first case has a wave height H of 0.8 m and a wave period T of 12 s, while in the second case the wave height H is equal to 1.2 m and the wave period T equal to 7.0 s. Both cases are investigated in a computational domain with constant water depth of $d = 10$ m which results in dimensionless depths kd of 0.55 and 1.05. Two vertical layers are applied to achieve a relative error below 5% for the second-order surface elevation amplitude (Table 2) and below 1% for the wave dispersion (Table 1). The model is applied with a grid cell size (Δx) of 1 m and 0.5 m for the first and second cases, respectively.

In Fig. 11, the normalised surface elevations η/α_0 for both cases are presented for a computational domain of five wave lengths. The waves are generated at the boundary of the computational domain by imposing either the first-order solutions (blue dashed lines) or both the first- and second-order solutions (red dashed lines). For the second-order wave generation the derived horizontal velocity components of Sections 3.1 (Eqs. (30)–(31)) and 3.2 (Eqs. (41)–(42)) are used to calculate the target horizontal velocity $u_{k,t}$ (Eq. (54)) for each layer, while for the radiation condition at the boundary the target surface elevation η_t is calculated using the derived second-order surface elevation amplitude (Eq. (40)).

As it can be deduced from Fig. 11, when only the first-order solutions are imposed, free spurious waves are introduced at the wave generation boundary. These spurious waves propagate with a different wave speed than the second-order wave, leading to the non-homogeneous surface profile that is observed. The maximum relative error in the surface elevation amplitude in the whole computational domain is 12.7% and 8.9% for the case with kd 0.55 and 1.05, respectively.

Free spurious waves have to be eliminated both in numerical models and experimental facilities, since they can affect significantly wave processes such as wave breaking, overtopping and runup. As it can be witnessed, when the derived second-order solutions are also imposed at the boundary, the resulting surface profiles are homogeneous in the whole domain and agree very well with the target theoretical profiles. For the second-order wave generation, the maximum relative error in the surface elevation amplitude is only 2.8% for $kd = 0.55$ and 1.7% for $kd = 1.05$. The fact that the error is smaller for the latter case can be justified by Fig. 5 where the ratios of second-order surface η_{02SW}/η_{02St} is 1.04 and 0.98 for kd values of 0.55 and 1.05, respectively.

Additionally, two cases of second-order bichromatic waves are also examined. As mentioned in Section 3.4, the wave-wave interaction of two harmonics with frequencies ω_m and ω_n forces a second-order wave group composed of four bound components, one sub-harmonic, $\omega_m - \omega_n$, and three super-harmonics, $2\omega_m$, $2\omega_n$ and $\omega_m + \omega_n$. These bound wave components play a important role on the wave transformation processes in shallow water (Madsen and Sørensen, 1993; Hamm et al., 1993). The bound super-harmonic components influence the shape and asymmetry of the waves, and consequently, the location of wave breaking, while the bound sub-harmonic component, which is also referred to as infra-gravity wave, is released after wave breaking and significantly contributes in coastal erosion, wave overtopping and wave penetration inside harbours.

The first bichromatic case (Table 5) is composed of two primary waves with wave heights $H_m = 0.6$ m and $H_n = 0.8$ m and wave periods

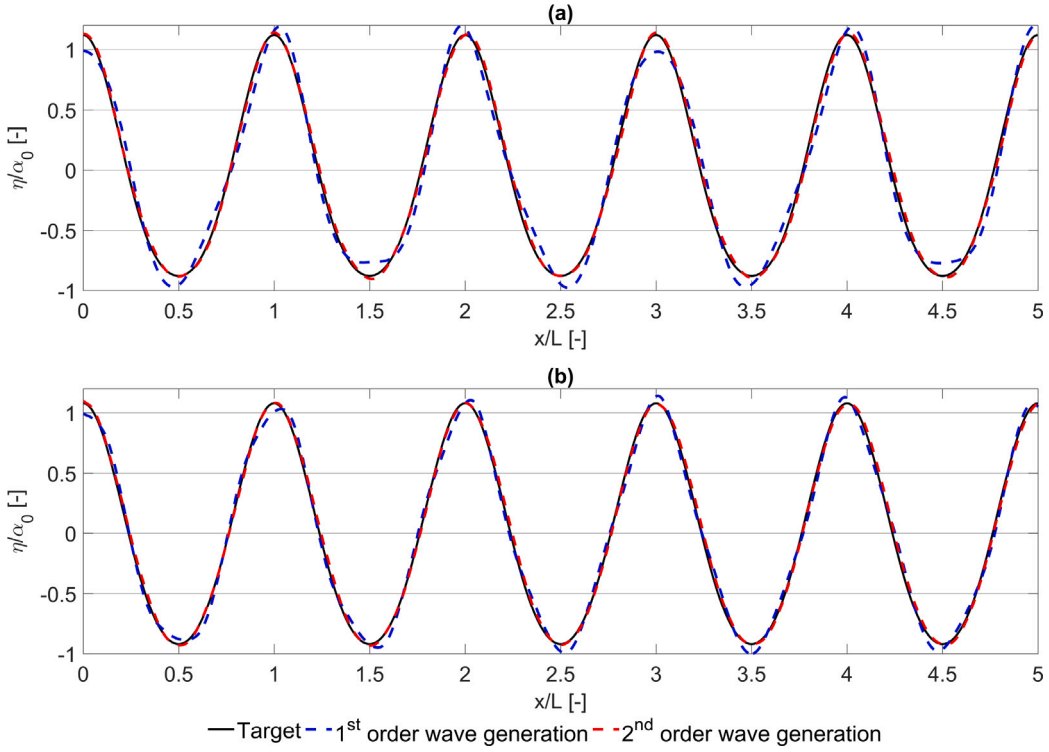

Fig. 11. Comparison between computed (dashed lines) and target (solid lines) normalised surface elevation η/α_0 for the case of second-order monochromatic waves with dimensionless depth (a) $kd = 0.55$ and (b) $kd = 1.05$. The waves are generated at the boundary of the computational domain using first- (blue dashed lines) and second-order (red dashed lines) wave generation.

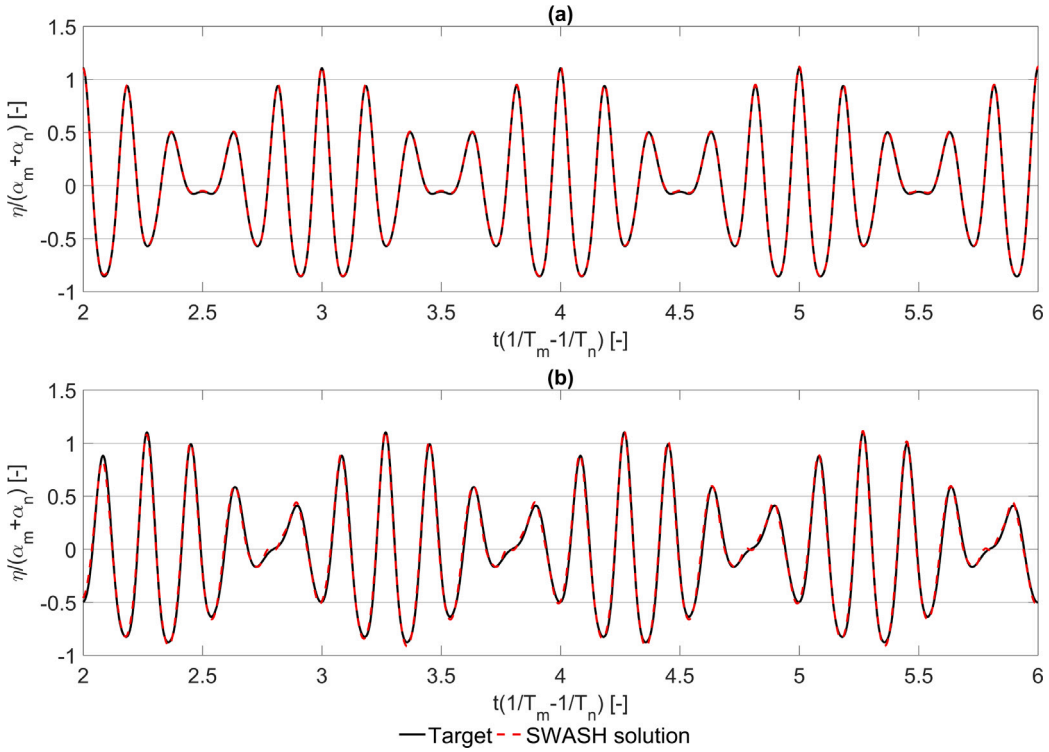

Fig. 12. Comparison between computed (dashed lines) and target (solid lines) normalised surface elevation for the case of second-order bichromatic wave with dimensionless depths $kd_m = 0.68$ and $kd_n = 0.55$ at a distance from the wave generation boundary (a) $x = 0$ m and (b) $x = 150$ m.

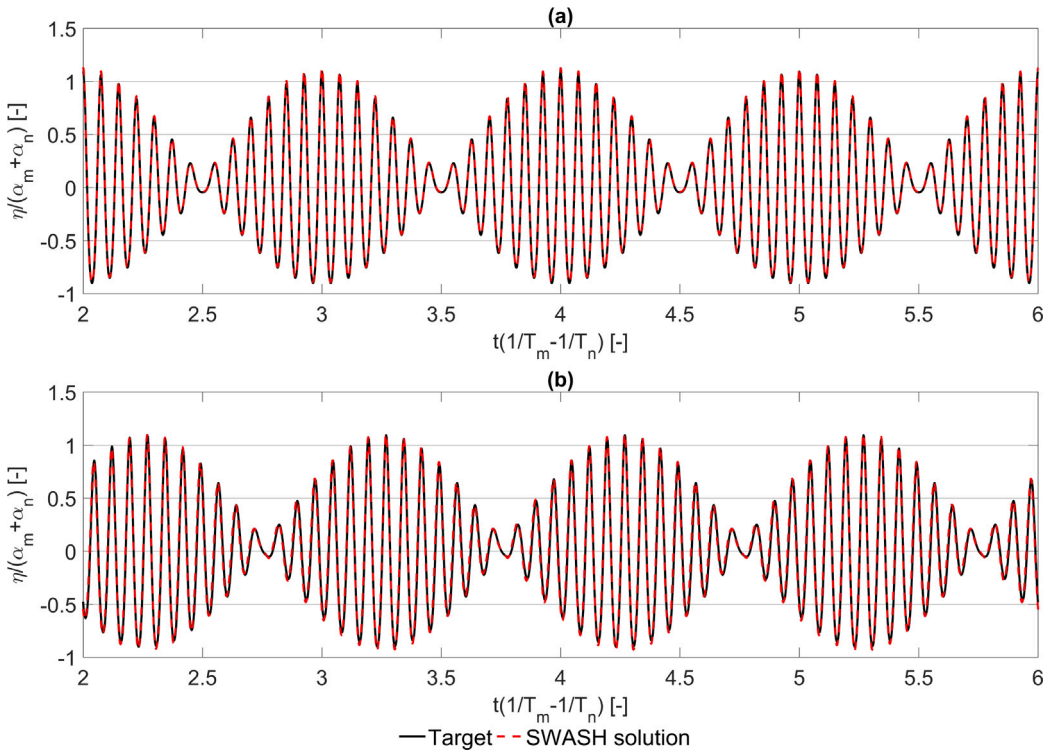

Fig. 13. Comparison between computed (dashed lines) and target (solid lines) normalised surface elevation for the case of second-order bichromatic wave with dimensionless depths $kd_m = 1.16$ and $kd_n = 1.05$ at a distance from the wave generation boundary (a) $x = 0$ m and (b) $x = 150$ m.

$T_m = 10.0$ s and $T_n = 12.0$ s, respectively. The second case considers slightly steeper waves with wave heights $H_m = 1.0$ m and $H_n = 1.2$ m and wave periods $T_m = 6.5$ s and $T_n = 7.0$ s, respectively. For both cases two vertical layers are applied while the waves propagate over a flat bottom with water depth of $d = 10$ m. As a result, the dimensionless depths are $kd_m = 0.68$ and $kd_n = 0.55$ for the first case and $kd_m = 1.16$ and $kd_n = 1.05$ for the second case, respectively.

In Figs. 12 and 13, the target (solid black lines) and computed (dashed red lines) surface elevations are presented normalised using the primary amplitudes α_m and α_n. The surface elevations are measured at two locations, one next to the wave generation boundary and one at a distance of 150 m (wg1 and wg2 in Fig. 9). To generate the waves in the numerical boundary of SWASH, six components are imposed, two for the primary waves and four for the bound waves, calculated using the derived second-order transfer functions of horizontal velocities and surface elevations of Section 3.4. The resulting profile is compared with the theoretical solutions given by Schäffer (1996) and Sand and Mansard (1986), where an excellent agreement can be noticed for both cases at all locations. It is noteworthy that the magnitude of transfer functions for the first case where shallower water waves interact is at least double compared to the second case where deeper water waves are investigated.

5. Conclusions

In this study, the non-hydrostatic governing equations of the multi-layer SWASH model have been analysed to define the linear and non-linear properties of the model when up to four vertical layers are applied. Tables have been defined, indicating dimensionless water depth ranges over which the model achieves the target accuracy depending on the number of layers employed. The derived solutions are also used to formulate higher-order hydraulic boundary conditions, targeting on improving and extending the wave generation capabilities of models based on non-hydrostatic equations.

First, a Stokes-type Fourier analysis on a flat bottom has been performed in order to define the first-, second- and third-order equations. Subsequently, by solving the system of equations, expressions have been derived for wave dispersion, surface elevation, horizontal and vertical velocities and non-hydrostatic pressure for linear and non-linear monochromatic waves. The derived solutions are then compared with the ones resulting from Stokes wave theory in order to determine the level of accuracy of the model.

From the linear analysis, it can be argued that the model can achieve excellent dispersion accuracy using a few vertical layers, since in the case of three layers the error stays below 1% up to a kd value of 16.41. However, the improvement in accuracy for the velocities and dynamic pressure is not as pronounced as for the wave dispersion. This is reflected in the limited range of dimensionless depths over which the relative error stays below 1% and 3%. From the non-linear analysis, a major improvement of the capability of the model to represent the Stokes second-order properties is noticed when a multi-layer layout is applied. The Stokes third-order surface component and the amplitude dispersion are also satisfactorily described by the governing equations of the model although for a smaller range of kd values than the second-order.

Additionally, the capability of the non-hydrostatic equations of SWASH model to describe the second-order sub-harmonic and super-harmonics resulted by wave-wave interaction of two first-order wave components has been examined. In general, for a multi-layer layout the model is capable of accounting for sub-harmonics forced by interactions between shallow water waves and intermediate-deep water waves, while for super-harmonics even by interactions between intermediate and deep water waves.

Subsequently, the derived expressions for horizontal velocities and free surface have been utilised to formulate weakly reflective boundary conditions to generate first-order monochromatic waves and second-order monochromatic and bichromatic waves.

The comparison of the normalised surface elevation and wave height, generated by imposing the first-order theoretical and derived

solutions, shows that the latter are able to accurately reproduce the linear target profiles. The use of the derived solutions as the target horizontal velocity in the weakly reflective wave generation boundary avoids the well-known sharp decrease in surface elevation and wave height at the first computational cells, resulting in a significantly better agreement with the target wave.

Regarding the second-order wave generation, the results demonstrate the benefits of implementing the derived expressions in the model for wave generation. The free spurious waves, that are introduced at the wave generation boundary by applying linear conditions, are eliminated by imposing both the first- and second-order derived solutions. Consequently, the resulting surface profiles are homogeneous and in very good agreement with the target theoretical profiles in the whole computational domain. Finally, the model's ability to accurately simulate the second-order bound wave components of bichromatic waves is noteworthy, as these components play an important role in wave transformation processes in shallow water. The model's ability to accurately generate and simulate these bound wave components will be valuable in predicting and understanding the impact of bound waves on coastal areas.

CRediT authorship contribution statement

Panagiotis Vasarmidis: Conceptualization, Methodology, Software, Validation, Writing – original draft. **Georgios Klonaris:** Methodology, Writing – review & editing. **Marcel Zijlema:** Software, Supervision, Writing – review & editing. **Vasiliki Stratigaki:** Supervision, Writing – review & editing. **Peter Troch:** Resources, Supervision, Writing – review & editing.

Declaration of competing interest

The authors declare that they have no known competing financial interests or personal relationships that could have appeared to influence the work reported in this paper.

Data availability

Data will be made available on request.

References

Ai, C., Jin, S., Lv, B., 2011. A new fully non-hydrostatic 3D free surface flow model for water wave motions. Internat. J. Numer. Methods Fluids 66 (11), 1354–1370. http://dx.doi.org/10.1002/fld.2317, URL: https://onlinelibrary.wiley.com/doi/10.1002/fld.2317.

Bai, Y., Cheung, K.F., 2013. Dispersion and nonlinearity of multi-layer non-hydrostatic free-surface flow. J. Fluid Mech. 726, 226–260. http://dx.doi.org/10.1017/jfm.2013.213.

Blayo, E., Debreu, L., 2005. Revisiting open boundary conditions from the point of view of characteristic variables. Ocean Model. 9 (3), 231–252. http://dx.doi.org/10.1016/j.ocemod.2004.07.001, URL: https://linkinghub.elsevier.com/retrieve/pii/S1463500304000447.

Brocchini, M., Peregrine, D.H., 1996. Integral flow properties of the swash zone and averaging. J. Fluid Mech. 317, 241–273. http://dx.doi.org/10.1017/S0022112096000742, URL: https://www.cambridge.org/core/product/identifier/S0022112096000742/type/journal{_}article.

Castro-Orgaz, O., Cantero-Chinchilla, F.N., Chanson, H., 2022a. Shallow fluid flow over an obstacle: higher-order non-hydrostatic modeling and breaking waves. Environ. Fluid Mech. 22 (4), 971–1003. http://dx.doi.org/10.1007/s10652-022-09875-0, URL: https://link.springer.com/10.1007/s10652-022-09875-0.

Castro-Orgaz, O., Cantero-Chinchilla, F.N., Hager, W.H., 2022b. High-order shallow water expansions in free surface flows: Application to steady overflow processes. Ocean Eng. 250, 110717. http://dx.doi.org/10.1016/j.oceaneng.2022.110717, URL: https://linkinghub.elsevier.com/retrieve/pii/S0029801822001688.

Castro-Orgaz, O., Hager, W.H., Katopodes, N.D., 2023. Variational models for nonhydrostatic free-surface flow: A unified outlook to maritime and open-channel hydraulics developments. J. Hydraul. Eng. 149 (7), http://dx.doi.org/10.1061/JHEND8.HYENG-13338, URL: https://ascelibrary.org/doi/10.1061/JHEND8.HYENG-13338.

Casulli, V., Stelling, G.S., 1998. Numerical simulation of 3D quasi-hydrostatic, free-surface flows. J. Hydraul. Eng. 124 (7), 678–686. http://dx.doi.org/10.1061/(ASCE)0733-9429(1998)124:7(678), URL: http://ascelibrary.org/doi/10.1061/%28ASCE%290733-9429%281998%29124%3A7%28678%29.

Dingemans, M.W., 1997. Water Wave Propagation Over Uneven Bottoms. In: Advanced Series on Ocean Engineering, vol. 13, World Scientific Publishing Company, http://dx.doi.org/10.1142/1241, URL: http://www.worldscientific.com/worldscibooks/10.1142/1241.

Dobrochinski, J.P., van Deyzen, A., Zijlema, M., van der Hout, A., 2023. Combining numerical tools to determine wave forces on moored ships. Coast. Eng. 179, 104224. http://dx.doi.org/10.1016/j.coastaleng.2022.104224, URL: https://linkinghub.elsevier.com/retrieve/pii/S0378383922001375.

Escalante, C., Fernández-Nieto, E.D., Garres-Díaz, J., Morales de Luna, T., Penel, Y., 2023. Non-hydrostatic layer-averaged approximation of Euler system with enhanced dispersion properties. Comput. Appl. Math. 42 (4), 177. http://dx.doi.org/10.1007/s40314-023-02309-7, URL: https://link.springer.com/10.1007/s40314-023-02309-7.

Gobbi, M.F., Kirby, J.T., Wei, G., 2000. A fully nonlinear Boussinesq model for surface waves. Part 2. Extension to o (kh) 4. J. Fluid Mech. 405, 181–210. http://dx.doi.org/10.1017/S0022112099007247, URL: https://www.cambridge.org/core/product/identifier/S0022112099007247/type/journal{_}article.

Green, A.E., Naghdi, P.M., 1976. A derivation of equations for wave propagation in water of variable depth. J. Fluid Mech. 78 (2), 237–246. http://dx.doi.org/10.1017/S0022112076002425, URL: https://www.cambridge.org/core/product/identifier/S0022112076002425/type/journal{_}article.

Hamm, L., Madsen, P.A., Peregrine, D., 1993. Wave transformation in the nearshore zone: A review. Coast. Eng. 21 (1–3), 5–39. http://dx.doi.org/10.1016/0378-3839(93)90044-9, URL: https://linkinghub.elsevier.com/retrieve/pii/0378383993900449.

Hibberd, S., Peregrine, D.H., 1979. Surf and run-up on a beach: a uniform bore. J. Fluid Mech. 95 (2), 323–345. http://dx.doi.org/10.1017/S002211207900149X, URL: https://www.cambridge.org/core/product/identifier/S002211207900149X/type/journal{_}article.

Higdon, R.L., 1987. Numerical absorbing boundary conditions for the wave equation. Math. Comp. 49 (179), 65. http://dx.doi.org/10.2307/2008250, URL: https://www.jstor.org/stable/2008250?origin=crossref.

Hu, K., Mingham, C., Causon, D., 2000. Numerical simulation of wave overtopping of coastal structures using the non-linear shallow water equations. Coast. Eng. 41 (4), 433–465. http://dx.doi.org/10.1016/S0378-3839(00)00040-5, URL: https://linkinghub.elsevier.com/retrieve/pii/S0378383900000405.

Kennedy, A.B., Kirby, J.T., Chen, Q., Dalrymple, R.A., 2001. Boussinesq-type equations with improved nonlinear performance. Wave Motion 33 (3), 225–243. http://dx.doi.org/10.1016/S0165-2125(00)00071-8, URL: https://linkinghub.elsevier.com/retrieve/pii/S0165212500000718.

Klonaris, G.T., Memos, C.D., Drønen, N.K., 2016. High-order Boussinesq-type model for integrated nearshore dynamics. J. Waterw. Port Coast. Ocean Eng. 142 (6), 04016010. http://dx.doi.org/10.1061/(ASCE)WW.1943-5460.0000349, URL: http://ascelibrary.org/doi/10.1061/%28ASCE%29WW.1943-5460.0000349.

Kobayashi, N., Otta, A.K., Roy, I., 1987. Wave reflection and run-up on rough slopes. J. Waterw. Port Coast. Ocean Eng. 113 (3), 282–298. http://dx.doi.org/10.1061/(ASCE)0733-950X(1987)113:3(282), URL: https://ascelibrary.org/doi/10.1061/%28ASCE%290733-950X%281987%29113%3A3%28282%29.

Kobayashi, N., Wurjanto, A., 1992. Irregular wave setup and run-up on beaches. J. Waterw. Port Coast. Ocean Eng. 118 (4), 368–386. http://dx.doi.org/10.1061/(ASCE)0733-950X(1992)118:4(368), URL: https://ascelibrary.org/doi/10.1061/%28ASCE%290733-950X%281992%29118%3A4%28368%29.

Liu, Z.B., Fang, K.Z., Cheng, Y.Z., 2018. A new multi-layer irrotational Boussinesq-type model for highly nonlinear and dispersive surface waves over a mildly sloping seabed. J. Fluid Mech. 842, 323–353. http://dx.doi.org/10.1017/jfm.2018.99, URL: https://www.cambridge.org/core/product/identifier/S002211201800099X/type/journal{_}article.

Lynett, P., Liu, P.L.-F., 2004a. A two-layer approach to wave modelling. Proc. R. Soc. Lond. Ser. A Math. Phys. Eng. Sci. 460 (2049), 2637–2669. http://dx.doi.org/10.1098/rspa.2004.1305, URL: https://royalsocietypublishing.org/doi/10.1098/rspa.2004.1305.

Lynett, P.J., Liu, P.L., 2004b. Linear analysis of the multi-layer model. Coast. Eng. 51 (5–6), 439–454. http://dx.doi.org/10.1016/j.coastaleng.2004.05.004.

Ma, G., Shi, F., Kirby, J.T., 2012. Shock-capturing non-hydrostatic model for fully dispersive surface wave processes. Ocean Model. 43–44, 22–35. http://dx.doi.org/10.1016/j.ocemod.2011.12.002.

Madsen, P.A., Bingham, H.B., Schäffer, H.A., 2003. Boussinesq-type formulations for fully nonlinear and extremely dispersive water waves: derivation and analysis. Proc. R. Soc. Lond. Ser. A Math. Phys. Eng. Sci. 459 (2033), 1075–1104. http://dx.doi.org/10.1098/rspa.2002.1067, URL: https://royalsocietypublishing.org/doi/10.1098/rspa.2002.1067.

Madsen, P.A., Murray, R., Sørensen, O.R., 1991. A new form of the Boussinesq equations with improved linear dispersion characteristics. Coast. Eng. 15 (4), 371–388. http://dx.doi.org/10.1016/0378-3839(91)90017-B, URL: https://linkinghub.elsevier.com/retrieve/pii/037838399190017B.

Madsen, P.A., Schäffer, H.A., 1998. Higher–order Boussinesq–type equations for surface gravity waves: derivation and analysis. Phil. Trans. R. Soc. A 356 (1749), 3123–3181. http://dx.doi.org/10.1098/rsta.1998.0309, URL: https://royalsocietypublishing.org/doi/10.1098/rsta.1998.0309.

Madsen, P.A., Sørensen, O.R., 1992. A new form of the Boussinesq equations with improved linear dispersion characteristics. Part 2. a slowly-varying bathymetry. Coast. Eng. 18 (3–4), 183–204. http://dx.doi.org/10.1016/0378-3839(92)90019-Q, URL: https://linkinghub.elsevier.com/retrieve/pii/037838399290019Q.

Madsen, P., Sørensen, O., 1993. Bound waves and triad interactions in shallow water. Ocean Eng. 20 (4), 359–388. http://dx.doi.org/10.1016/0029-8018(93)90002-Y, URL: https://linkinghub.elsevier.com/retrieve/pii/002980189390002Y.

Méhauté, B., 1976. An Introduction to Hydrodynamics and Water Waves. Springer Berlin Heidelberg, Berlin, Heidelberg, http://dx.doi.org/10.1007/978-3-642-85567-2, URL: http://link.springer.com/10.1007/978-3-642-85567-2.

Memos, C.D., Klonaris, G.T., Chondros, M.K., 2016. On higher-order Boussinesq-type wave models. J. Waterw. Port Coast. Ocean Eng. 142 (1), 04015011. http://dx.doi.org/10.1061/(ASCE)WW.1943-5460.0000317, URL: http://ascelibrary.org/doi/10.1061/%28ASCE%29WW.1943-5460.0000317.

Nwogu, O., 1993. Alternative form of Boussinesq equations for nearshore wave propagation. J. Waterw. Port Coast. Ocean Eng. 119 (6), 618–638. http://dx.doi.org/10.1061/(ASCE)0733-950X(1993)119:6(618), URL: http://ascelibrary.org/doi/10.1061/%28ASCE%290733-950X%281993%29119%3A6%28618%29.

Peregrine, D.H., 1967. Long waves on a beach. J. Fluid Mech. 27 (4), 815–827. http://dx.doi.org/10.1017/S0022112067002605, URL: https://www.cambridge.org/core/product/identifier/S0022112067002605/type/journal{_}article.

Peregrine, D., 1972. Equations for water waves and the approximation behind them. In: Waves on Beaches and Resulting Sediment Transport. Elsevier, pp. 95–121. http://dx.doi.org/10.1016/B978-0-12-493250-0.50007-2, URL: https://linkinghub.elsevier.com/retrieve/pii/B9780124932500500072.

Rijnsdorp, D.P., Hansen, J.E., Lowe, R.J., 2018. Simulating the wave-induced response of a submerged wave-energy converter using a non-hydrostatic wave-flow model. Coast. Eng. 140 (May), 189–204. http://dx.doi.org/10.1016/j.coastaleng.2018.07.004, URL: https://linkinghub.elsevier.com/retrieve/pii/S0378383917306440.

Rijnsdorp, D.P., Ruessink, G., Zijlema, M., 2015. Infragravity-wave dynamics in a barred coastal region, a numerical study. J. Geophys. Res.: Oceans 120 (6), 4068–4089. http://dx.doi.org/10.1002/2014JC010450, URL: http://doi.wiley.com/10.1002/2014JC010450.

Rijnsdorp, D.P., Smit, P.B., Zijlema, M., 2014. Non-hydrostatic modelling of infragravity waves under laboratory conditions. Coast. Eng. 85, 30–42. http://dx.doi.org/10.1016/j.coastaleng.2013.11.011, https://linkinghub.elsevier.com/retrieve/pii/S0378383913001944.

Rijnsdorp, D.P., Smit, P.B., Zijlema, M., Reniers, A.J., 2017. Efficient non-hydrostatic modelling of 3D wave-induced currents using a subgrid approach. Ocean Model. 116, 118–133. http://dx.doi.org/10.1016/j.ocemod.2017.06.012, URL: https://linkinghub.elsevier.com/retrieve/pii/S1463500317301014.

Rijnsdorp, D.P., Wolgamot, H., Zijlema, M., 2022. Non-hydrostatic modelling of the wave-induced response of moored floating structures in coastal waters. Coast. Eng. 177, 104195. http://dx.doi.org/10.1016/j.coastaleng.2022.104195, URL: https://linkinghub.elsevier.com/retrieve/pii/S0378383922001089.

Sand, S.E., Mansard, E., 1986. Reproduction of higher harmonics in irregular waves. Ocean Eng. 13 (1), 57–83. http://dx.doi.org/10.1016/0029-8018(86)90004-1, URL: https://linkinghub.elsevier.com/retrieve/pii/0029801886900041.

Schäffer, H.A., 1996. Second-order wavemaker theory for irregular waves. Ocean Eng. 23 (1), 47–88. http://dx.doi.org/10.1016/0029-8018(95)00013-B, URL: https://linkinghub.elsevier.com/retrieve/pii/002980189500013B.

Skjelbreia, L., 1959. Gravity Waves: Stokes' Third Order Approximation Tables of Functions. Council on Wave Research,the Engineering Foundation, URL: https://searchworks.stanford.edu/view/1168731.

Smit, P., Janssen, T., Holthuijsen, L., Smith, J., 2014. Non-hydrostatic modeling of surf zone wave dynamics. Coast. Eng. 83, 36–48. http://dx.doi.org/10.1016/j.coastaleng.2013.09.005.

Stelling, G., Zijlema, M., 2003. An accurate and efficient finite-difference algorithm for non-hydrostatic free-surface flow with application to wave propagation. Internat. J. Numer. Methods Fluids 43 (1), 1–23. http://dx.doi.org/10.1002/fld.595.

Suzuki, T., Altomare, C., Veale, W., Verwaest, T., Trouw, K., Troch, P., Zijlema, M., 2017. Efficient and robust wave overtopping estimation for impermeable coastal structures in shallow foreshores using SWASH. Coast. Eng. 122 (January), 108–123. http://dx.doi.org/10.1016/j.coastaleng.2017.01.009, https://linkinghub.elsevier.com/retrieve/pii/S0378383916302435.

Suzuki, T., Hu, Z., Kumada, K., Phan, L., Zijlema, M., 2019. Non-hydrostatic modeling of drag, inertia and porous effects in wave propagation over dense vegetation fields. Coast. Eng. 149, 49–64. http://dx.doi.org/10.1016/j.coastaleng.2019.03.011, URL: https://linkinghub.elsevier.com/retrieve/pii/S0378383917304179.

Svendsen, I.A., 2005. Introduction to Nearshore Hydrodynamics. In: Advanced Series on Ocean Engineering, vol. 24, WORLD SCIENTIFIC, http://dx.doi.org/10.1142/5740, URL: https://www.worldscientific.com/worldscibooks/10.1142/5740.

Svendsen, I.A., Madsen, P.A., 1984. A turbulent bore on a beach. J. Fluid Mech. 148, 73–96. http://dx.doi.org/10.1017/S0022112084002251, URL: https://www.cambridge.org/core/product/identifier/S0022112084002251/type/journal{_}article.

Vasarmidis, P., Stratigaki, V., Suzuki, T., Zijlema, M., Troch, P., 2019. Internal wave generation in a non-hydrostatic wave model. Water 11 (5), 986. http://dx.doi.org/10.3390/w11050986, URL: https://www.mdpi.com/2073-4441/11/5/986.

Vasarmidis, P., Stratigaki, V., Suzuki, T., Zijlema, M., Troch, P., 2021. On the accuracy of internal wave generation method in a non-hydrostatic wave model to generate and absorb dispersive and directional waves. Ocean Eng. 219, 108303. http://dx.doi.org/10.1016/j.oceaneng.2020.108303, URL: https://linkinghub.elsevier.com/retrieve/pii/S002980182031218X.

Wang, G., Liang, Q., Zheng, J., Wan, P., 2019. A new multilayer nonhydrostatic formulation for surface water waves. J. Coast. Res. 35 (3), 693. http://dx.doi.org/10.2112/JCOASTRES-D-18-00022.1, URL: https://bioone.org/journals/journal-of-coastal-research/volume-35/issue-3/JCOASTRES-D-18-00022.1/A-New-Multilayer-Nonhydrostatic-Formulation-for-Surface-Water-Waves/10.2112/JCOASTRES-D-18-00022.1.full.

Wang, G., Zheng, J., Liang, Q., 2018. Accuracy of depth-integrated nonhydrostatic wave models. Ocean Eng. 149, 217–225. http://dx.doi.org/10.1016/j.oceaneng.2017.12.015, URL: https://linkinghub.elsevier.com/retrieve/pii/S0029801817307370.

Wei, G., Kirby, J.T., Grilli, S.T., Subramanya, R., 1995. A fully nonlinear Boussinesq model for surface waves. Part 1. Highly nonlinear unsteady waves. J. Fluid Mech. 294, 71–92. http://dx.doi.org/10.1017/S0022112095002813, URL: https://www.cambridge.org/core/product/identifier/S0022112095002813/type/journal{_}article.

Whitham, G.B., 1999. Linear and Nonlinear Waves. John Wiley & Sons, Inc., Hoboken, NJ, USA, http://dx.doi.org/10.1002/9781118032954, URL: http://doi.wiley.com/10.1002/9781118032954.

Yamazaki, Y., Cheung, K.F., Kowalik, Z., 2011. Depth-integrated, non-hydrostatic model with grid nesting for tsunami generation, propagation, and run-up. Internat. J. Numer. Methods Fluids 67 (12), 2081–2107. http://dx.doi.org/10.1002/fld.2485, URL: http://doi.wiley.com/10.1002/fld.2485.

Yang, Z.T., Liu, P.L.-F., 2020. Depth-integrated wave–current models. Part 1. Two-dimensional formulation and applications. J. Fluid Mech. 883, A4. http://dx.doi.org/10.1017/jfm.2019.831, URL: https://www.cambridge.org/core/product/identifier/S0022112019008310/type/journal{_}article.

Zhao, B., Duan, W., Ertekin, R., 2014. Application of higher-level GN theory to some wave transformation problems. Coast. Eng. 83, 177–189. http://dx.doi.org/10.1016/j.coastaleng.2013.10.010, URL: https://linkinghub.elsevier.com/retrieve/pii/S037838391300166X.

Zijlema, M., 2020. Computation of free surface waves in coastal waters with SWASH on unstructured grids. Comput. & Fluids 213, 104751. http://dx.doi.org/10.1016/j.compfluid.2020.104751, URL: https://linkinghub.elsevier.com/retrieve/pii/S0045793020303212.

Zijlema, M., Stelling, G.S., 2005. Further experiences with computing non-hydrostatic free-surface flows involving water waves. Internat. J. Numer. Methods Fluids 48 (2), 169–197. http://dx.doi.org/10.1002/fld.821, URL: http://doi.wiley.com/10.1002/fld.821.

Zijlema, M., Stelling, G., 2008. Efficient computation of surf zone waves using the nonlinear shallow water equations with non-hydrostatic pressure. Coast. Eng. 55 (10), 780–790. http://dx.doi.org/10.1016/j.coastaleng.2008.02.020, URL: https://linkinghub.elsevier.com/retrieve/pii/S0378383908000380.

Zijlema, M., Stelling, G., Smit, P., 2011. SWASH: An operational public domain code for simulating wave fields and rapidly varied flows in coastal waters. Coast. Eng. 58 (10), 992–1012. http://dx.doi.org/10.1016/j.coastaleng.2011.05.015.